MODELLING GEOMETRY AND MECHANICS OF DISORDERED NANOMATERIALS

by

NICHOLAS WINTER

(Under the Direction of Xianqiao Wang)

ABSTRACT

For materials with nanoscale features control of mass, geometry, and size/scale result in significantly different mechanical behaviors for chemically identical materials. These three independent variables arise together in nanoporous materials and nanofibrous materials where the samples have density that is variable and lower than the theoretical maximum, a geometry that is defined by occupied space and void space, and most notably geometric features that are within the nanoscale. Observations of size-effects on the strength, toughness, and failure mode of nanoscale metals have been made and one pressing topic in nanomechanics is the continuation of experimental, computational, and theoretical investigations of size effects to piece together an encompassing theory. The following work is centered on the discussion around the role of size on a material's mechanical behavior with a focus on nanoporous materials and nanofibrous materials.

INDEX WORDS: Mechanics, molecular dynamics, finite element, porous materials, fibrous materials, computational methods

MODELLING GEOMETRY AND MECHANICS OF DISORDERED NANOMATERIALS

by

NICHOLAS WINTER

B.S. BCHE, University of Georgia, 2016

A Thesis Submitted to the Graduate Faculty of The University of Georgia in Partial Fulfillment of the Requirements for the Degree

MASTER OF SCIENCE

ATHENS, GEORGIA

2018

MODELLING GEOMETRY AND MECHANICS OF DISORDERED NANOMATERIALS

by

NICHOLAS WINTER

Major Professor:	Xianqiao Wang
Committee:	Eric Freeman
	Zhong-Ru Xie

Electronic Version Approved:

Suzanne Barbour
Dean of the Graduate School
The University of Georgia
December 2018

DEDICATION

Mary Lisa Filla, Robert Filla, Alexandria Winter. Love you all.

Janice Filla, Gary Filla, Kevin Winter. Wish you were here.

ACKNOWLEDGEMENTS

Dr. Xianqiao Wang, Dr. Liuyang Zhang, Dr. Mir Jalil Razavi, Ning Liu, and Matthew Becton.

Thank you.

TABLE OF CONTENTS

LIST OF TABLES

LIST OF FIGURES

CHAPTER 1 INTRODUCTION

In 1959 Richard Feynman endorsed the advancement of nanoscience in a well celebrated speech “There is plenty of room at the bottom”. This is very evident in the case of materials with nanoscale features where control of mass, geometry, and size/scale result in significantly different mechanical behaviors from chemically identical materials. These three independent variables arise together in nanoporous materials and nanofibrous materials where the samples have density that is variable and lower than the theoretical maximum density, a geometry that is defined by occupied space and void space, and most notably geometric features that are within the nanoscale. The following work is centered on the discussion around the role of size on a material's mechanical properties with a focus on nanoporous materials and nanofibrous materials.

The first intuition's about size effects are thought to date back to Leonardo da Vinci when he observed that "a cord is so much stronger ... as it is shorter. [1]" The first known implication of an inverse relationship between size and strength. This was later refuted by Galileo Galilei while he was developing the concept of stress [2]. Mariotte continued the discussion in the direction of what is now known as the concept of defect probability with his conclusion that "a long rope and a short one always support the same weight unless there may happen to be some faulty place in which it will break sooner than in a shorter [rope].[3]" A conversation that was of little concern until the 1921 paper by A.A. Griffith, the father of fracture mechanics, titled *The Phenomena of Rupture and Flow in Solids* [4] where he postulated that "very small solids of

given form, e.g., wires or fibers, might be expected to be stronger than larger ones, as there must in such cases be some additional restriction on the size of the flaws. In the limit, in fact, a fiber consisting of a single line of molecules must possess the theoretical molecular tensile strength." This paper generated a wealth of study from well-known scientists leading to the "weakest-link" model created by Pierce [5] and refined by Tippet [6, 7], Fischer [7], Fréchet [8], and von Mises [9]. Then in 1939 Weibull concretely devised the thesis of this study with his statistical theory which gave the probability relationship between size frequency and strength [10]. This work of-course led to the study of size effects at large scales with size and strength being linked by the probability of flaws. It wasn't until 1994 that Fleck discovered an entirely different size-effect phenomena in the rupture of solids when studying microscopically thin copper wires under tensile and torsional loads. They observed that flow stresses in thinner copper wires increased with no other explanation than the wire diameter [11]. He observed that flow stresses in thinner copper wires increased with no other explanation than the wire diameter. Since 1994 experimental and computational evidence for the inverse relationship between strength and the characteristic size at small length scales has been increasing.

Nanoporous and nanocolumnar metals, gold and copper, have been used extensively to study the effect of size on strength and have found repeatedly, across a large range of sizes, that smaller is stronger [12-19]. The observations of size-effects in metals are being made and the current purpose of this field is to continue the experimental, computational, and theoretical investigation of these effects to piece together an encompassing theory. Currently the key factors being investigated are structure, sample size, initial dislocation density, surface roughness, and the potential-energy landscape for dislocation motion [20-24]. In this thesis nanoporous and nanofibrous materials are investigated through geometric modelling and mechanical loading simulations. This work is meant to contribute to the field of mechanical materials at the

nanoscale where classical theories of elasticity and plasticity are not in agreement with experimental and computational data due to size effects. We perform computational modelling to study the mechanics of nanoscale materials, supply further calculations for the materials science community, report scaling law models that fit our data, and describe the nature of plastic deformations that were observed from simulation. We find that the scaling law for relativity density and mechanical parameters such as elastic moduli, strength, and toughness for nanoporous materials can be represented by an Ashby-Gibson type equation but the scaling is more dramatic. We observe that nucleation and transmission of cracks and flaws are starved in nanoporous materials for a lack of degrees of freedom leading to stronger foams. Plastic yielding is also seen to persist at high-strains beyond what would typically be expected for mesoscale foams leading to increases in toughness. The scope of the study includes a common brittle material (silicon), a common metal (aluminum), and leads up to study of porous cellulose nanofibers but this work is not yet complete.

CHAPTER 2 EFFECT OF PORE GEOMETRY ON THE MECHANICS OF NANOPOROUS SILICON SLABS

Nanoporous silicon has been a powerful material in computing, sensing, and catalysis. The capability to design silicon materials with desired mechanical properties is paramount to their reliability and serviceability. With the availability of advanced nanoscopic design techniques including ion etching [25], chemical vapor deposition [26], and atomic manipulation via scanning tunneling electron microscopy [27], tailoring the design of nanostructures is not only possible, but the fabrication processes to achieve these nanostructures continue to increase in precision and viability. Nanopores bestow useful characteristics upon materials such as high surface-area to volume ratios, increased catalytic power [28], high yield-strength to weight ratios [29], and strain reversibility [30]. To bring further resolution to the mechanical characteristics of nanoporous silicon we perform molecular dynamics simulations and study the effects of ligament thickness, relative density, and pore geometry on the mechanical properties and plasticity of nanoporous silicon, thereby determining its Young's modulus, ultimate strength, and toughness as well as the scaling laws and failure mechanisms. Results show that pore geometry dictates stress accumulation inside the structure, leading to distinct failure signatures, such as stretching-dominated, bending-dominated, or stochastic failure signatures. The nanostructure is also found to drive or mute size effects such as "smaller is stronger" and "smaller is ductile" while the porosity of the material correlates to standard Ashby-Gibson scaling laws for Young's modulus and ultimate strength.

Pore geometry has been shown to heavily influence the mechanical properties of the diatom's cell-wall [31] and represents the larger end of the scale for nanoporous silicon with pore sizes reaching up to ~1500 nm (Figure 2.1(a)). At the smallest end of the scale is MCM-41 (Mobil Composition of Matter No. 41, a family member of nanoporous silicon materials) with nanopores as small as 2 nm (Figure 2.1(c)) [32]. Nanoporous silicon with pore sizes ranging from 2 nm to 1,500 nm have been widely used in applications including the connection of catalytic components such as enzymes [33], anodes in lithium ion batteries [34], resistive random-access memory in computers (RRAM) [35], and scaffolding for cell encapsulation and implantation where mechanical properties are of high concern [36]. Understanding how the mechanical properties of nanoporous silicon may be altered by structural design is important for these applications. For instance, one promising technique in RRAM is electromechanical coupling using mechanical strains to induce a change in the magnetic order of a material and is a possible solution for decreasing the energy needed to store information [35]. The magnetic order of nanoporous silicon in this scenario is dependent on the absolute strain that it is experiencing and therefore the material's elastic modulus is an important design parameter for sizing and developing nanoporous silicon materials that satisfy the engineering constraints.

In previous studies by Garcia et al. tension studies on nanoporous silica with a rectangular mesh geometry and constant void volume between various sized models have been simulated. They found that the failure mechanism of nanoporous silica is correlated with relative density and ligament thickness and can change from crack propagation dominated failure, to failure characterized by the competition between crack propagation and shear mechanisms, and even failure fitting the criteria of ductile rupture [37, 38]. Garcia et al. also show that as ligament size is decreased the ductility of nanoporous silica increases, its elastic modulus decreases, its strength decreases, and that its toughness has a complex relationship with ligament thicknesses

below 27 angstroms [37-39]. These studies shed light on the nature of the connection between mechanical properties of nanoporous silicon and size but by maintaining a constant void volume while changing the size of ligaments the relative density must be changed and so the observations cannot conclude whether the cause of changes in mechanical response are due to relative density or size effects. To further these investigations, we tease apart the effects of relative density and ligament thickness to make clear how each design parameter changes the mechanical response of nanoporous silicon and include effects of pore geometry on the mechanics of nanoporous silicon as well. To better understand how one might manipulate the mechanical properties of nanoporous silicon by controlling its nanoporous structure, we model nanoporous silicon with various relative densities, ligament thicknesses, and pore geometries under tensile loadings and discuss the results.

2.1 Geometry of Porous Silicon Slabs

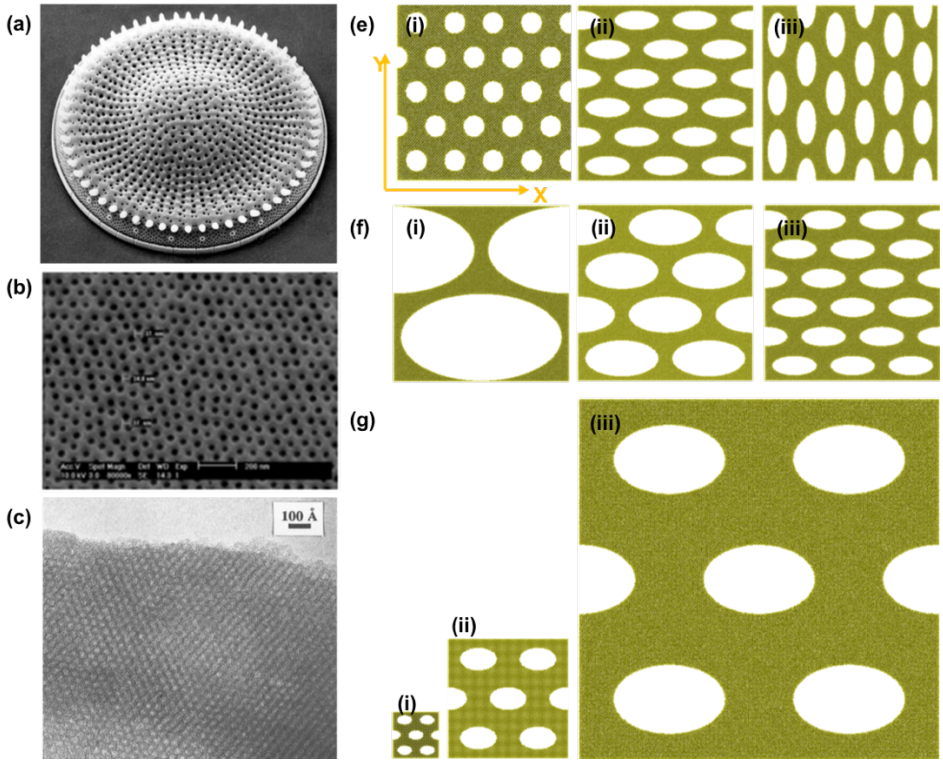

Figure 2. 1: (a) Diatom showing their porous silica structure (b) a TEM picture of nanoporous silicon produced via lithography (c) TEM photograph of calcined nanoporous silicon known as MCM-41. (d) Nanoporous silicon with a constant ligament thicknesses of 3.5 nm (i) Staggered Circles (SC) (ii) Horizontal Ellipses (H-ellipses) and (iii) Vertical Ellipses (V-ellipses); (e) H-ellipse nanoporous silicon with ligament thicknesses of 3.5 nm and relative densities of (i) 0.313 (ii) 0.495 and (iii) 0.67. (f) H-ellipse nanoporous silicon with relative densities of 0.71 and ligament thicknesses of (i) 1.74 nm (ii) 4.47 nm and (iii) 13.42 nm

Here, models with dimensions $43nm \times 43nm \times 7nm$ are used to study the mechanical properties and failure patterns of nanoporous silicon slabs with different pore geometries. We propose three different pore patterns with the same relative density: staggered circles (circles), staggered horizontal ellipses (H-ellipses, whose major axis is aligned with the loading direction), and staggered vertical ellipses (V-ellipses, whose major axis is orthogonal to the loading direction), Figure 2.1(d). The major axes of ellipses range in size from 3.5 nm to 34.3 nm while the minor axes range from 1.9 nm to 18.2 nm and the circle diameters range from 1.9 nm to 26.1 nm, all ellipses have an eccentricity ~0.8. Of equal importance to the mechanical properties of porous materials is their stress-strain relationship with relative density therefore we propose a set of models for each porous geometry with various relative densities (Figure 2.1(e)). In addition to pore pattern and relative density, ligament size has been shown to play an important role in the mechanical behaviors of other nanoporous materials such as nanoporous gold [40] and nanoporous aluminum [41], giving us reason to investigate the effect of ligament size on the mechanical properties of nanoporous silicon as well with representative models (Figure 2.1(f)). Computational models used to study effect of ligament size on the mechanical properties of nanoporous silicon are $7nm$ thick in the z-direction with the x- and y-axes lengths varying from $9.5nm \times 9.5nm$ to $73nm \times 73nm$. For the purpose of clarity, we define the relative density, $\overline{\rho} = \frac{\rho_*}{\rho_b}$ of the models as the ratio of the density of the chosen porous model, ρ_*, to the

density of the bulk material, ρ_b. Ligament thickness is measured as the width of nanoporous silicon struts where adjacent pores are closest together.

2.2 Modelling Mechanics of Silicon using Molecular Dynamics

For this work, molecular dynamics simulations based on the open-source code LAMMPS are performed to investigate the mechanical behavior of nanoporous silicon [42]. Through preliminary tensile-test simulations on bulk silicon using the environmentally dependent interatomic potential (EDIP) [43], Stillinger-Weber (SW) Potential [44], and Tersoff potential [45], we found that the Stillinger-Weber potential shows the best accuracy in bulk modulus and elastic modulus with comparison to experimental data [46]. Therefore, we choose the SW potential to perform the relevant MD simulations. The details of SW potential are tabulated as follows:

$$E = \sum_i \sum_{j>i} \varphi_2(r_{ij}) + \sum_i \sum_{j\neq i} \sum_{k>j} \varphi_3(r_{ij}, r_{ik}, \theta_{ijk}) \tag{2.1}$$

$$\varphi_2(r_{ij}) = A_{ij}\epsilon_{ij}\left[B_{ij}\left(\frac{\sigma_{ij}}{r_{ij}}\right)p_{ij} - \left(\frac{\sigma_{ij}}{r_{ij}}\right)q_{ij}\right] e^{\left(\frac{\sigma_{ij}}{r_{ij}-a_{ij}\sigma_{ij}}\right)} \tag{2.2}$$

$$\varphi_3(r_{ij}, r_{ik}, \theta_{ijk}) = \lambda_{ijk}\epsilon_{ijk}\left[\cos\theta_{ijk} - \cos\theta_{oijk}\right]^2 e^{\left(\frac{\gamma_{ij}\sigma_{ij}}{r_{ij}-a_{ij}\sigma_{ij}}\right)} e^{\left(\frac{\gamma_{ik}\sigma_{ik}}{r_{ik}-a_{ik}\sigma_{ik}}\right)} \tag{2.3}$$

where E is the energy, φ_2 is a two-body term describing the interaction of two atoms (ex: Si_1Si_2) and φ_3 is a three-body term representing the interaction of three atoms (ex: $Si_1Si_2Si_3$). The summations in the formula are over all neighbors j and k of atom i. During tensile simulations all silicon models are loaded in the same lattice direction.

2.3 Effect of Pore Geometry on Stress-Strain Response and Material Failure

In relevant studies, pore design is shown to affect the mechanical behaviors such as stiffness, strength, and recoverability of porous materials including porous polymers [47], hydroxyapatite bioceramics [48], and aluminum oxide ceramics [49]. Figure 2.2 shows a side by side comparison of three nanoporous silicon models (staggered circles, H-ellipses, and V-ellipses) with different relative densities but the same ligament thicknesses of $d = 3.5$ nm. All models are colored by per atom stress in the loading direction [1 0 0] and each color gradient has the same range (0 to 0.35 $GPa \times nm^3$).

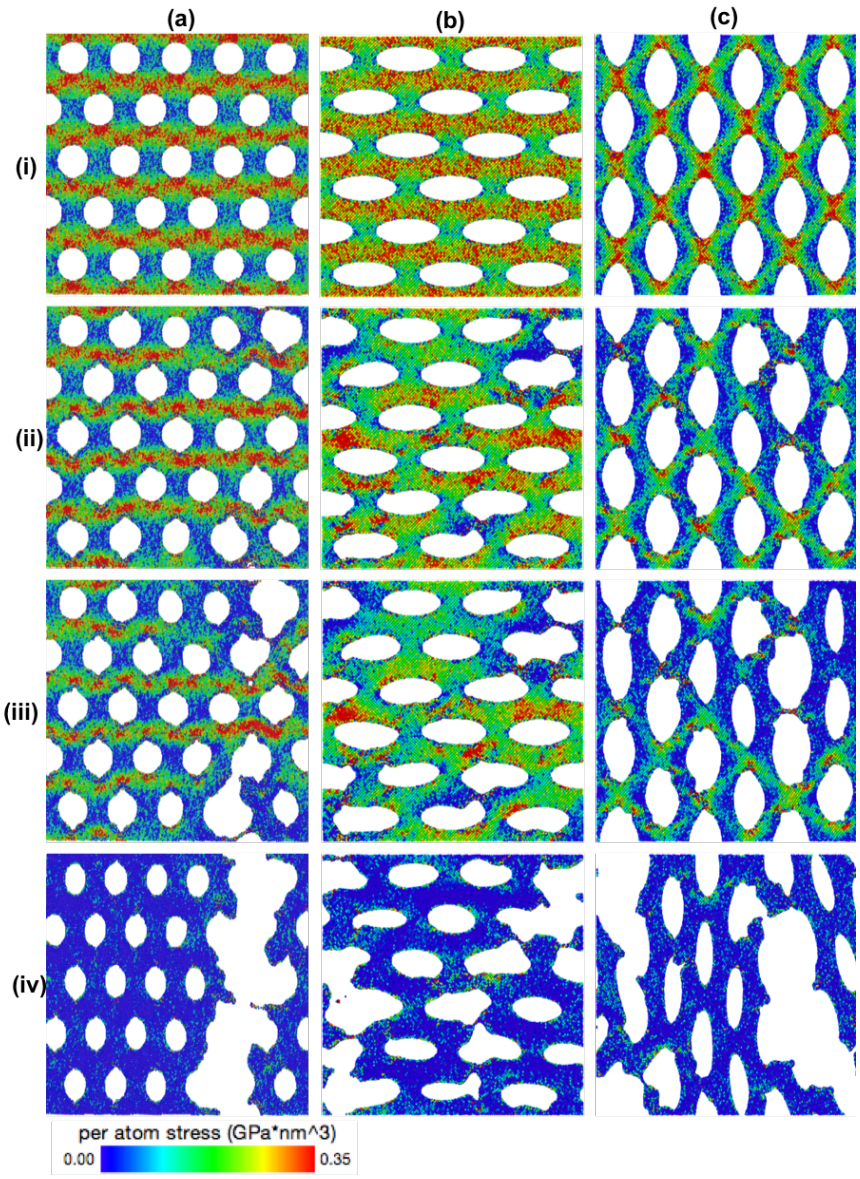

Figure 2. 2: Frame by frame failure of nanoporous silicon having different pore geometries/orientations. Models are loaded in the [1 0 0] direction and atoms are colored by per atom stress in the [1 0 0] direction. (a) Nanoporous silicon with staggered circular pores (row (i) strain of 0.11). (b) Nanoporous silicon with H-ellipse pore geometry (row (i) strain of 0.13). (c) Nanoporous silicon with V-ellipse geometry (row (i) strain of 0.16). Snapshots begin at peak stress/strain and end when stress reached zero.

The first row in Figure 2.2 shows the stress concentration and distribution in each model just before yielding. The proceeding snapshots capture the failure of each model and show that each nanoporous silicon design experiences ligament failure initiated by cracking and completed

by ligaments necking to ductile rupture. The distribution and concentration of stress for each atom within each structure can be observed further in Figure 2.3 where each model is pictured at the same loading (848.2 nN) and only atoms experiencing a per atom stress over 0.35 $GPa \times nm^3$ are shown.

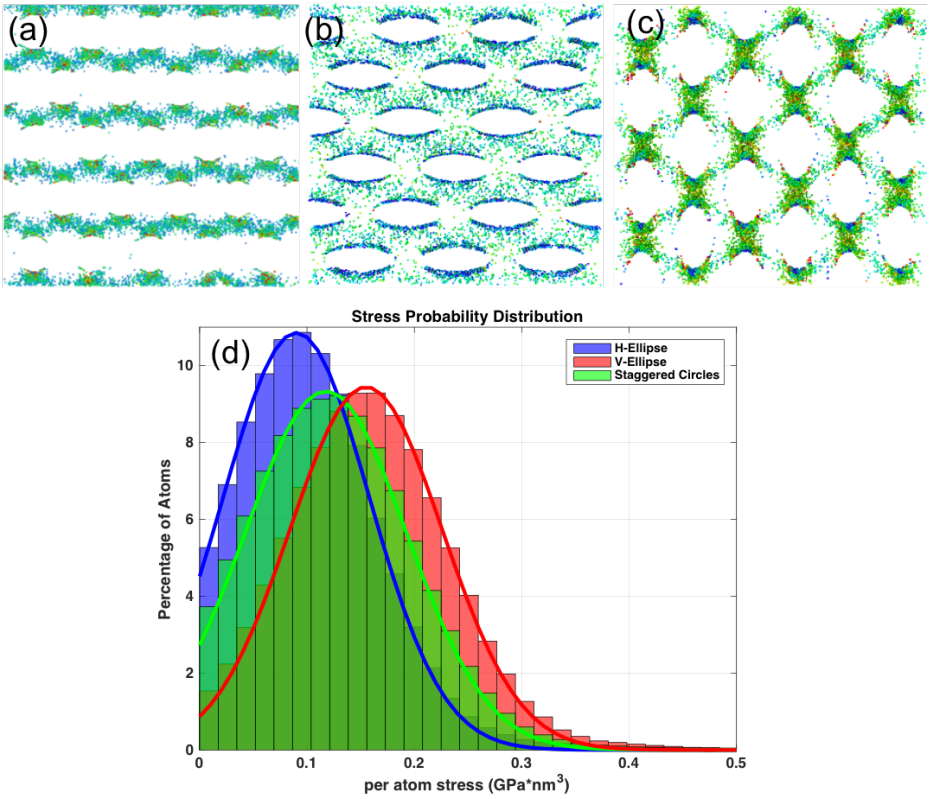

Figure 2. 3: snapshots corresponding to Figure 3 row (i), where only atoms experiencing a per atom stress of 0.35 $GPa \times nm^3$ or higher are shown. (a) Staggered Circles Nanoporous silicon (b) H-Ellipse Nanoporous silicon (c) V-Ellipse Nanoporous silicon (d) histogram showing the percentage of atoms experiencing a per atom stress between 0 and 0.5 $GPa \times nm^3$

With the ligament thickness and strain rate being kept fixed, pore geometry becomes the major design variable and Figure 2.3 shows that the horizontal ellipse configuration allows stresses to distribute evenly throughout the structure (Figure 2.3(b)) with a low average per atom stress of 0.158 $GPa \times nm^3$ (obtained from the stress distribution curve Figure 2.3(d)). With per atom stresses being distributed evenly and remaining comparatively low, nanoporous silicon

with horizontal ellipses shows great strength and a high elastic modulus with respect to the other two (Table 2.1).

Tabel 2. 1 Comparison of mechanical properties for nanoporous silicon with different pore geometry

Pore Geometry	Young's Modulus (GPa)	Ultimate Strength (GPa)	Toughness (MJ/m^3)
H-ellipses	67.8	7.4	557.8
Staggered circles	58.7	5.6	336.4
V-ellipses	25.0	4.2	453.4

Once pore geometry is changed to staggered circles, stresses become more concentrated within the structure raising the average per atom stress to 0.176 $GPa \times nm^3$. With the average stress climbing (driven by the number of atoms able to carry large stresses falling) the elastic modulus and strength of nanoporous silicon are effectively lowered. The concentration of stresses increases further after changing the orientation of the elliptical pattern from horizontal ellipses to vertical ellipses. The stresses in the vertical ellipse nanoporous structure are highly concentrated; the average per atom stress reaches 0.183 $GPa \times nm^3$ within this structure resulting in a further decrease of ultimate strength and elastic modulus.

From Table 2.1 it can be seen that Young's modulus, ultimate strength and toughness of nanoporous silicon are dramatically affected by changing the pore geometry and pore orientation, while keeping ligament size and relative density unchanged. For example, the horizontal ellipse nanoporous silicon exhibits an elastic modulus that is slightly greater than staggered circle nanoporous silicon, 1.2 times greater, but much greater than vertical ellipse

nanoporous silicon at 2.7 times. In contrast, although strength and elastic modulus are the lowest of the nanoporous structures, it has a toughness that is higher than that of nanoporous silicon with staggered circles showing that changing the nanostructure does not always induce a monotonic increase or decrease in all mechanical properties.

2.4 Effect of Relative Density on Stress-Strain Response

The mechanical properties and scaling laws of macroporous materials and nanoporous materials have been shown to be dependent on pore geometry [47, 48], ligament thickness [20, 50], relative density [50, 51], and grain size [52-54]. Experimental and computational studies also reveal that strength and elastic moduli of nanoporous materials scale differently than microporous and macroporous materials with respect to relative density [50, 51, 55]. Figure 2.4 shows the uniaxial stress-strain curves for nanoporous structures with constant ligament thickness and variable relative density.

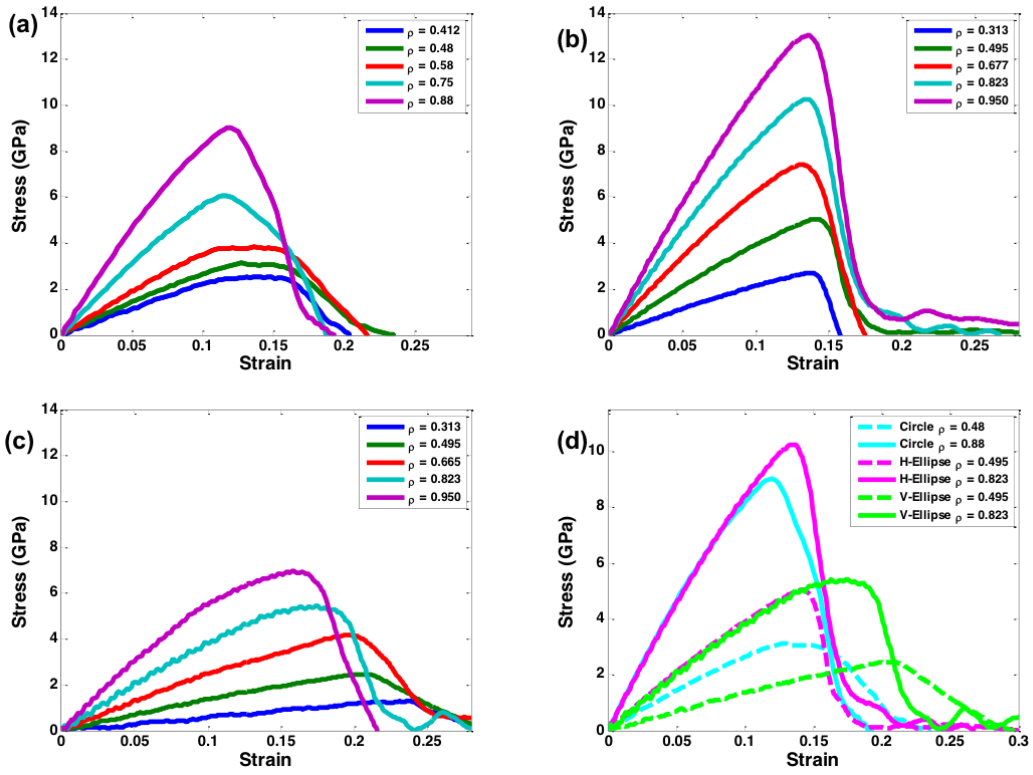

Figure 2. 4: Stress-strain relationship of nanoporous silicon versus the relative density under three different pore patterns: (a) staggered circles; (b) staggered horizontal ellipses; (c) staggered vertical ellipses; (d) a comparison among these three cases. Ligament thickness = 3.5 nm.

In Figure 2.4, upon the initiation of deformation the stress builds up fairly linearly until the material yields. After reaching the ultimate strength, σ_u, the stress decreases with increasing strain as the material's ligaments begin to tear and rupture. The elastic modulus E, the ultimate strength σ_u, and the toughness κ of a given nanoporous silicon model are measured from the stress-strain curves and used to develop scaling laws.

The deformation of cellular solids can be dominated by bending or stretching; the failure regime is dictated by the geometry of the lattice and its connectivity. The strength and elastic modulus of an ideal stretching-dominated structure scale linearly with relative density $E \sim \overline{\rho}$ and $\sigma_u \sim \overline{\rho}$ [56] while bending-dominated and stochastic architectures scale as $E \sim \overline{\rho}^2$ and $E \sim \overline{\rho}^3$ respectively [57]. The yield strength and modulus of 3D open-cell bending dominated structures,

such as honeycombs or octahedral lattices, scale as $\sigma_u = 0.3\sigma_b\overline{\rho}^{1.5}$ and $E = E_b\overline{\rho}^2$ [58, 59]. Nanoporous silicon with horizontal ellipse pores behaves as a marginally stretching-dominated structure with its young's modulus scaling as $E \propto \overline{\rho}^{1.5}$ and strength scaling as $\sigma_u \propto \overline{\rho}^{1.5}$ (Figure 2.5 (a) and 2.5 (b)).

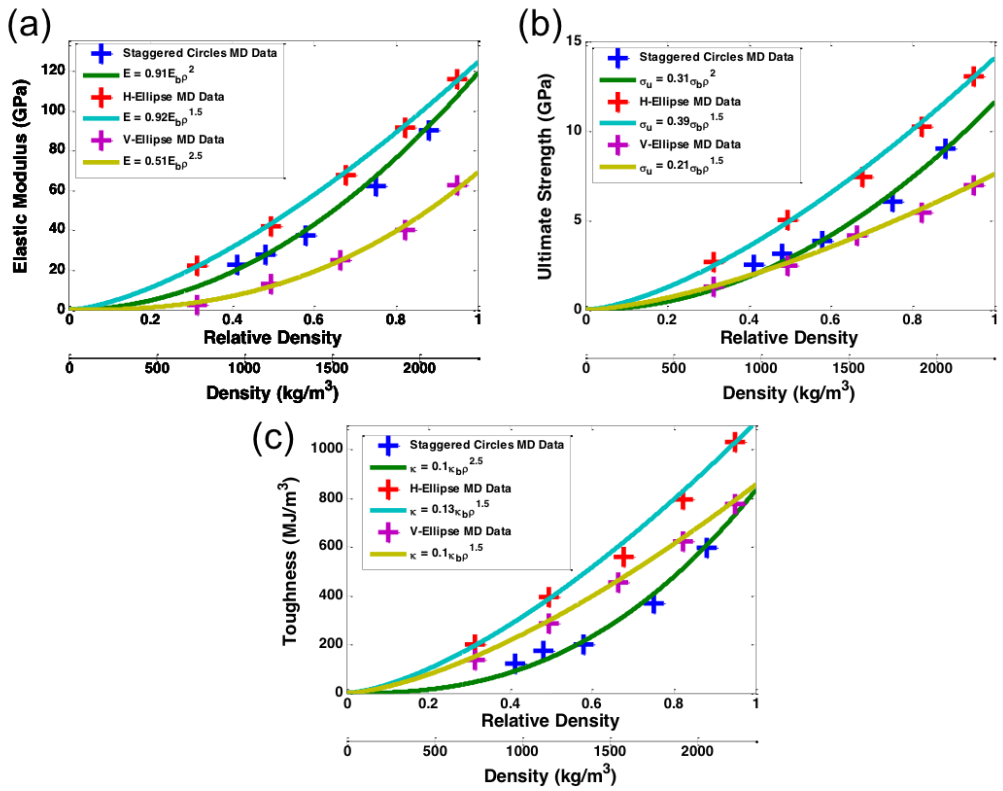

Figure 2. 5: Semi-empirical correlations of material properties versus relative density. (a) elastic modulus; (b) ultimate strength; (c) toughness. Cross-hairs represent MD data and is fitted by a scaling curve. Ligament thickness = 3.5 nm.

The stretching-dominated signature provides nanoporous silicon with the highest values of stiffness, strength, and toughness to weight ratios of all models and complete failure of the structure happens at a strain of ~0.15 for all relative densities and ligament thicknesses. The architecture of horizontal ellipse nanoporous silicon is accompanied with a highly engaged structure where stress disseminates evenly under tension. In the generic Equations (2.4) and (2.5)

the proportionality constant C_1 is less than 1 at a nominal value of 0.92 and the proportionality constant C_2 is greater than 0.3 at a nominal value of 0.39 for the horizontal ellipse nanoporous silicon.

$$E = E_b C_1 \overline{\rho}^n \tag{2.4}$$

$$\sigma_u = \sigma_b C_2 \overline{\rho}^n \tag{2.5}$$

nanoporous silicon with staggered circular pores exhibits a bending-dominated failure scaling signature with Young's modulus scaling as $E \propto \overline{\rho}^2$ and strength scaling as $\sigma_u \propto \overline{\rho}^2$. In this regime, nanoporous silicon's strength, stiffness, and toughness are lower than that of horizontal ellipse nanoporous silicon by 13.42%, 24.32%, and 39.7% respectively and the strain at failure is between 0.10 and 0.14 (Figure 2.5(a)) depending on relative density and ligament thickness. Structurally, the staggered circle pore geometry carries stress fairly evenly under tension in the [1 0 0] direction. In the generic Equations (2.4) and (2.5) the proportionality constants C_1 and C_2 for nanoporous silicon with staggered circles are calculated to be 0.91 and 0.32 respectively. Nanoporous silicon with vertical ellipse pores is found to behave as a stochastic structure with young's modulus scaling as $E \propto \overline{\rho}^{2.5}$ and strength scaling as $\sigma_u \propto \overline{\rho}^{1.5}$. The strength and stiffness to weight ratios of the vertical ellipse nanoporous silicon are lower than both the horizontal ellipse models and staggered circles models. However, the toughness is higher than that of the staggered circles nanoporous silicon due to a very large strain at failure, between 0.17 and 0.25. The constants C_1 and C_2 for nanoporous silicon with vertical ellipses are calculated to be 0.51 and 0.21 respectively, which is very low compared to the other models tested here. An Ashby plot in terms of stiffness and material density is provided in Figure 2.6 to show the comparison between the nanoporous silicon simulations and known materials.

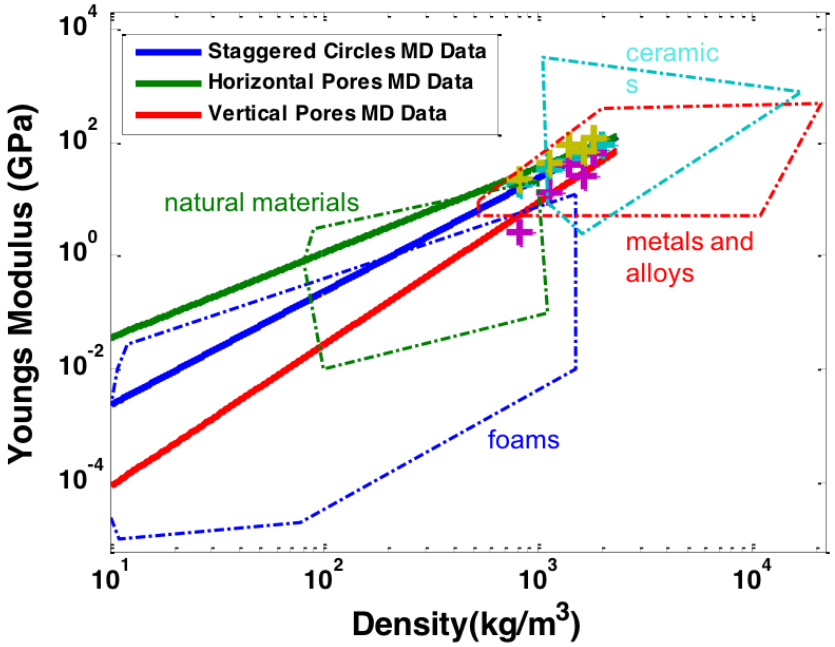

Figure 2. 6: Material property space plot of Young's modulus versus density, with dotted regions showing the phase space of common structural materials.

The vertical ellipse and horizontal ellipse nanoporous silicon data represent the minimum and maximum values of stiffness from our simulations, with horizontal ellipse nanoporous silicon about twice as stiff as vertical ellipse nanoporous silicon at high densities. Though, due to horizontal ellipse nanoporous silicon scaling more ideally than vertical ellipse nanoporous silicon it is ~10 times stiffer at a relative density of 0.3 and predicted to be ~100 times stiffer at ultralight relative densities of $\overline{\rho} \sim 0.01$. Horizontal ellipse nanoporous silicon is predicted to scale into a new niche in material property space at densities below 90 kg/m^3 or $\overline{\rho} = 0.04$ while other nanoporous silicon models are predicted to scale into the existing foam material property space at very low densities.

Toughness (κ) is taken as the area under the stress strain curves (Figure 2.5) from zero strain until ultimate strain at failure and describes how much energy the nanoporous silicon

models absorb during a full stretch to failure. Models are found to scale as $\kappa \sim \overline{\rho}^{1.5}$ for both horizontal ellipse and vertical ellipse nanoporous silicon and $\kappa \sim \overline{\rho}^{2.6}$ for staggered circles nanoporous silicon (Figure 2.5(c)). Scaling constants, C_3 in Equation (2.6), are found to be very low ~0.1 for each model.

$$\kappa = \kappa_b C_3 \overline{\rho}^n \tag{2.6}$$

Toughness, stiffness, and strength in nanoporous silicon are found to be uncoupled from each other such that a stronger, stiffer model may not be tougher than its weaker, less stiff counterpart or a stronger, tougher model may not be as stiff as its weaker, less tough counterpart. For example, as seen in Figure 2.5, staggered circle nanoporous silicon is stiffer than vertical ellipse nanoporous silicon for all relative densities, is stronger than vertical ellipse nanoporous silicon for relative densities greater than 0.44, but is not as tough as vertical ellipse nanoporous silicon for any relative density below 0.96.

2.5 Effect of Ligament Thickness on Stress-Strain Response

At the nanoscale, materials usually exhibit size effects such as "smaller is weaker" in nanocrystalline metals [60], "smaller is ductile" in metallic glasses and ceramics [61], and "smaller is stronger" in monocrystalline metals [29, 40, 50, 62]. Although the Young's modulus has not been shown, to the best of our knowledge, to be correlated with ligament thickness, strength and toughness have been seen to scale with ligament thickness as a power relationship i.e. $Z(d) \sim cd^n$, where Z may represent ultimate strength or toughness, c and n are experimentally determined coefficients, and d is the ligament thickness. No strong, nonlinear curves are found in our data which covers the ligament thickness range of 1.7376nm to

13.423nm and so we plot our scaling laws for the Young's modulus, ultimate strength, and toughness of nanoporous silicon linearly as $Z(d) = bd + c$.

Young's modulus, ultimate strength, and toughness are calculated from the stress-strain curves in Figure 2.7 and plotted in Figure 2.8.

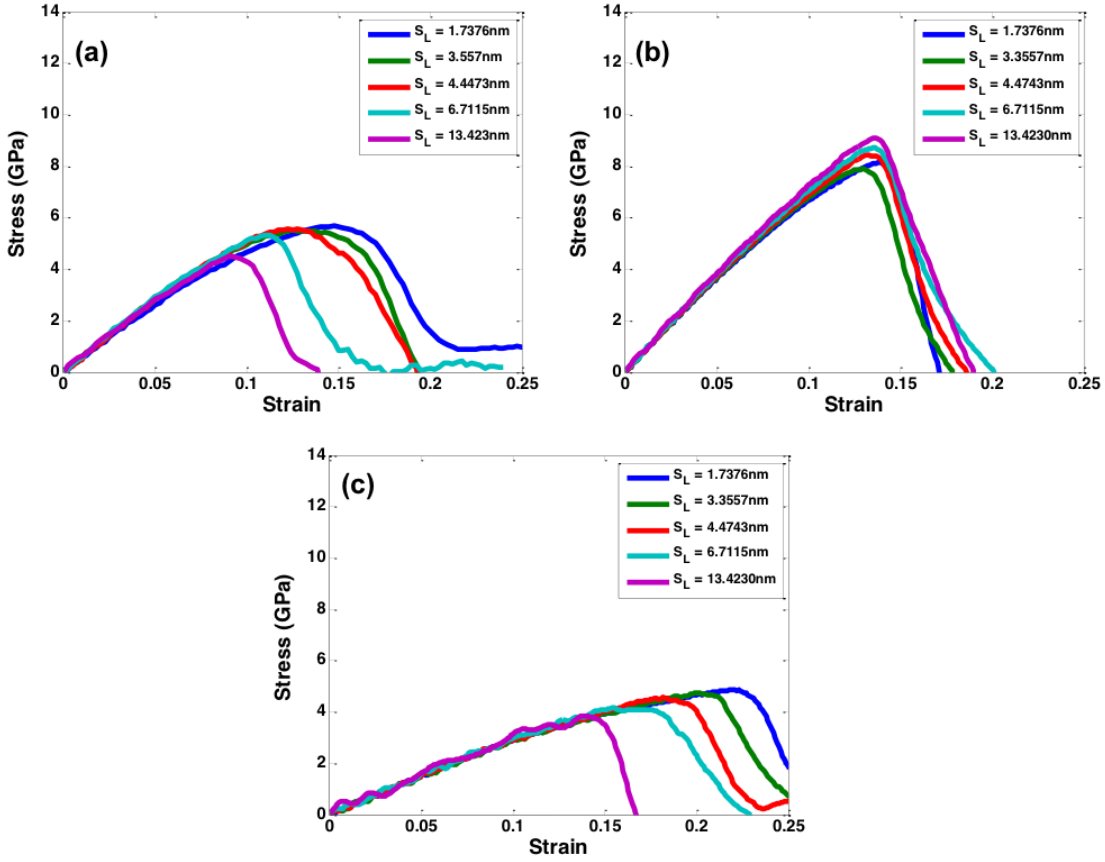

Figure 2. 7: Stress-strain relationship of nanoporous silicon versus the ligament size under the same relative density: (a) staggered circles; (b) staggered horizontal ellipses; (c) staggered vertical ellipses. Relative density = 0.67.

The linear region of each stress-strain curve is taken to measure the Young's modulus, the peak of each curve is taken as the ultimate strength, and the area under each curve from zero strain until the strain at failure is taken as the toughness. Interestingly, horizontal ellipse nanoporous silicon behaves unlike staggered circle nanoporous and vertical ellipse nanoporous

silicon for all three attributes (strength, toughness, and ductility) with respect to ligament thickness. In the case of nanoporous silicon with vertical ellipses and staggered circles the relationships "smaller is stronger" and "smaller is ductile" are observed. Under constant relative density, our simulations predict that nanoporous silicon with vertical ellipses gains 170 MPa in ultimate strength for every nanometer that the average ligament thickness is reduced and nanoporous silicon with staggered circular pores gains 105 MPa per nanometer reduction in ligament thickness. However, the simulations show that nanoporous silicon can lose ~100 MPa in ultimate strength for every nanometer that the average ligament thickness is reduced if the pore geometry is changed to H-ellipse nanoporous silicon. As ligament diameter approaches zero the strain at failure for V-ellipse nanoporous silicon approaches 0.227 while the strain at failure for staggered circles approaches 0.149. However, in the case of H-ellipse nanoporous silicon smaller is neither stronger nor more ductile. Strength decreases as ligament thickness decreases and ductility does not change very obviously as ligament thickness changes. In sum, from Figure 9 it is clear to show that size effects exist for ultimate strength, toughness, and ultimate strain while for the Young's modulus the size effect can be negligible.

2.6 Chapter Summary

Our simulations show that the scaling laws of nanoporous silicon are dependent on pore geometry, pore orientation, relative density, and ligament thickness. Decreasing relative density results in decreases in all mechanical properties where: Young's modulus scales as $E \propto \rho^n$ with n ranging from an almost stretching-dominated signature of 1.5 to a stochastic signature of 2.5, strength scales as $\sigma_u \propto \rho^n$ with n ranging from 1.5 to 2, and toughness scales as $\kappa \propto \rho^n$ with n ranging from 1.5 to 2.6. Toughness in nanoporous silcon is found to be uncoupled from Young's modulus and strength such that a stronger, stiffer model may not be tougher than its

weaker, less stiff counterpart. Ligament thickness plays a negligible effect on the Young's modulus of nanoporous silicon in the range of 1.7 nm to 13.4 nm; however trends are strong enough to report for ultimate strength, toughness, and ductility. Size effects are not consistent for nanoporous silicon models with different nanostructures: nanoporous silicon with staggered circular pores and vertical elliptical pores become stronger and more ductile as ligament thickness decreases while nanoporous silicon with horizontal elliptical pores becomes weaker as ligament thickness decreases and shows no discernable change in ductility as ligament thickness changes. Nanostructure can shape the stress distribution leading to changes in mechanical properties and material failure.

CHAPTER 3 EFFECT OF LIGAMENT THICKNESS AND RELATIVE DENSITY ON NANOPOROUS ALUMINUM

Aluminum is prized for its low density, ability to resist corrosion, and large deformations before plasticity [63, 64]. These qualities have made aluminum an important material in construction and transportation. Now with techniques capable of generating nanoporous aluminum and other nanoporous metals, namely dealloying, it is of considerable importance to investigate their properties.

A critical phenomena observed in these nanostructures is that smaller size leads to greater strength. The prediction that size may effect mechanical strength was first posed by A.A. Griffith in 1921 [4]. 73 years later Fleck *et al*. sparked interest in the field when they observed this effect in copper wires with cross-sections ~10 μm in diameter experiencing tensile and torsional loading[65]. Later, Biener *et al*. found a yield strength for nanoporous gold that was 10 times higher than Ashby-Gibson scaling laws predicted and raised the question whether the scaling laws deduced from macroscopic foams can be applied to nanoporous materials [66]. Volkert *et al*. also reported that yield stresses of gold nanocolumns increase strongly as column diameter decreases [20]. To *et al*. studied size effects in nanoporous aluminum using molecular dynamics simulations of nanoporous aluminum models created by deleting overlapping spherical regions in a cube [67]. Sun *et al*. used molecular dynamics simulations on more realistic nanoporous metal models created by phase-field methods in order to study failure mechanisms and scaling laws of nanoporous gold [50]. In 2014 Suarez *et al*. fabricated the first sample of dealloyed nanoporous aluminum [68]. Here we further the efforts by studying the effects of density and

ligament diameter on the mechanical properties and failure mechanisms of bicontinuous, open-cell, nanoporous aluminum structures using phase-field methods to generate nanoporous geometries and molecular dynamics simulations to predict mechanical responses. We develop scaling laws for Young's modulus, yield strength, ultimate strength, and toughness with respect to relative density and ligament diameter. It is demonstrated that failure in nanoporous aluminum under tensile stress begins with plastic deformation at ligament junctions observed by the nucleation of dislocation loops on the free surfaces of nanoporous aluminum which propagate into the body of the structure's ligaments facilitating atomic motion along slip planes.

3.1 Geometry of Bicontinuous, Open-cell, Nanoporous Aluminum

One method for creating nanoporous metals is dealloying which creates a geometry very similar to the geometries observed during the spontaneous separation of immiscible fluids. With that in mind, the Cahn-Hilliard equations for the separation of two immiscible fluids are used to create the bicontinuous, open-cell, aluminum structures modelled here [50, 69, 70]. The Cahn-Hilliard equations are as follows and can be solved on a simple cubic lattice grid with numerical integration of time:

$$\frac{\partial u}{\partial t} = \nabla^2 \left[\frac{df(u)}{du} - \theta \nabla^2 u \right] \tag{3.1}$$

$$\frac{df(u)}{du} = \frac{1}{4}(u^2 - 1)^2 \tag{3.2}$$

Here, $u(x, y, z, t)$ is the order-parameter whose value determines whether a point represents component A or component B of the mixture. The overall behavior of the Cahn-Hilliard equation

is determined by the free energy functional, Equation (3.2), which determines what values of u are stable; in this case there are two stable values of u, -1 and +1. To make it clear, the free energy equation determines that -1 and +1 represent domains that are pure in either component A or component B. θ controls the thickness of the boundary layer that divides a domain pure in component A from a domain pure in component B.

Initially the value of u for the discrete, regularly-spaced nodes are randomly chosen and assigned a positive or negative value close to zero. The assigned value determines whether a point is richer in component A or component B of a binary mixture. By solving the Cahn-Hilliard equation the binary mixture is separated into domains which are pure in each component. After the separation, one component is removed and the remaining material is a bicontinuous, open-cell structure. Figure 3.1(a) shows the dynamic evolution of the mixture separation process in 2-dimensions governed by the Cahn-Hilliard equation. The final ratio of component A to component B in the mixture is a predictable quantity because it strongly depends on the initial conditions. At the beginning of each simulation every node in the phase field is assigned an initial order-parameter value. For example, if 60% are assigned positive values at the beginning then one would correctly expect that the number of +1 nodes at the end of the separation would be close to 60%. Figure 3.1(b) shows six nanoporous aluminum models with the relative density as 0.36, 0.44, 0.54, 0.65, 0.74, and 0.84 with an average ligament diameter of 5.0 nm. The relative density is defined as the ratio of the porous sample's density to the density of bulk aluminum; the average ligament diameter is calculated by taking multiple cross sections of each sample, measuring the characteristic length of each ligament, and then averaging the measurements together.

Besides the relative density of the nanoporous structure, the size of the pure domains in the structure are directly proportional to how long the system is allowed to separate, therefore in

order to control the average ligament diameters in the nanoporous models with a fixed relative density of interest we need to adjust the simulation time. Figure 3.1(c) shows four models with the average ligament diameters of 3.11 nm, 5.64 nm, 7.47 nm, and 9.88 nm with relative densities around 40%. After the creation of the bicontinuous domains, the Al atoms of interest are populated into the domains with positive values to generate their coordinates in the 3D structure as depicted in Figure 3.1 (b) and (c).

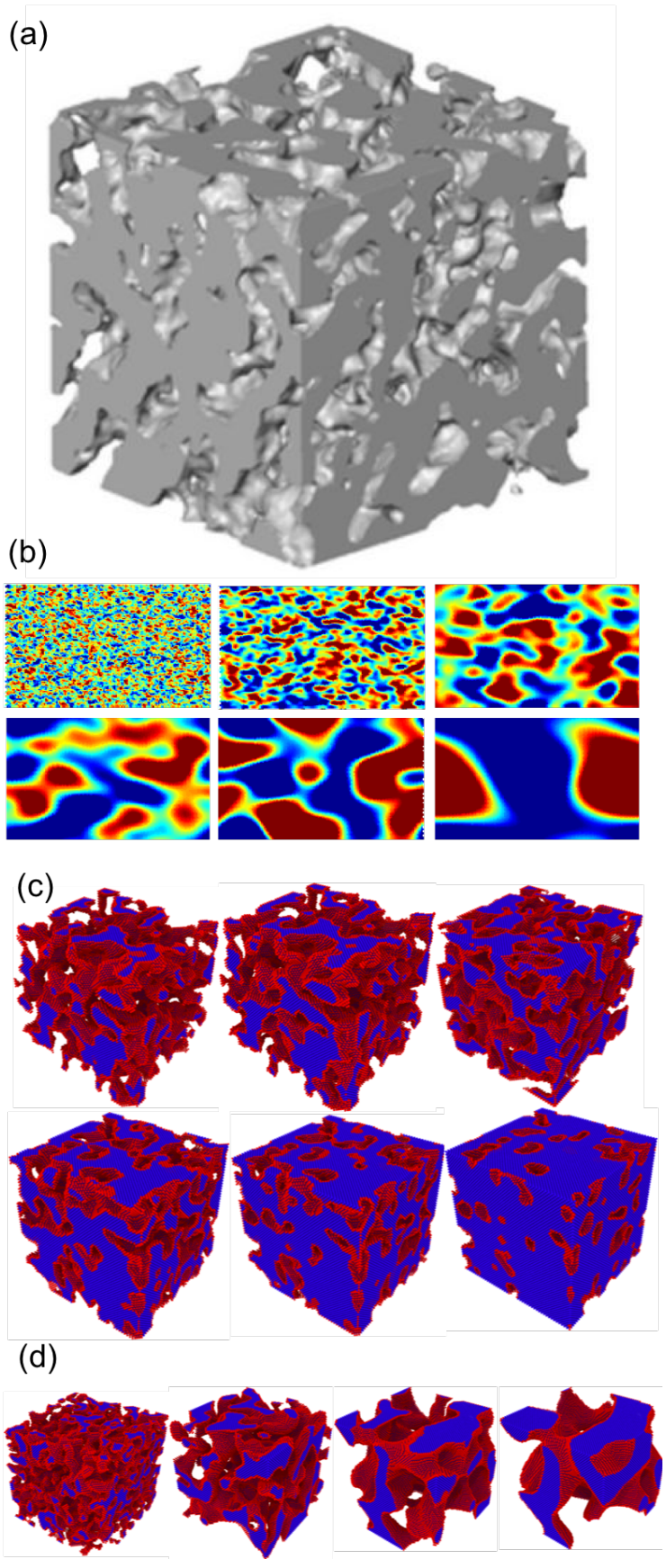
(a)
(b)
(c)
(d)

Figure 3. 1: (a) X-ray tomography of nanoporous aluminum prepared by dealloying Al_2Mg_3 [71]. (b) Time evolution of a 2D binary fluid based on Cahn-Hillaird equation. Simulation time steps corresponding to each photo, from left to right, are 20, 60, 180, 540, 1620, and 4860. (c) Nanoporous aluminum models with the same average ligament diameter but different relative densities 0.36, 0.44, 0.54, 0.65, 0.74, and 0.84. (d) Nanoporous aluminum models with the same relative density but different ligament diameters 3.11nm, 5.64nm, 7.47nm, and 9.88nm.

3.2 Modelling Mechanics of Aluminum using Molecular Dynamics

Molecular dynamics simulations based on the open-source code LAMMPS are performed to investigate the mechanical behavior of the nanoporous aluminum [42]. In order to accurately capture the electron cloud effect of metallic materials, an embedded atom method (EAM) potential is adopted to describe the interatomic forces between aluminum atoms in our model, which is detailed as follows [72]:

$$E_i = F_\alpha\left(\sum_{j\neq i}\rho\beta\left(r_{ij}\right)\right) + \frac{1}{2}\sum_{j\neq i}\varphi_{\alpha\beta}\left(r_{ij}\right) \tag{3.3}$$

E_i is the potential energy of atom i, F_α is the embedding energy which is a function of the atomic electron density ρ, $\varphi_{\alpha\beta}$ is a pair potential interaction, and α and β are the element types of atoms i and j. The $20nm \times 20nm \times 20nm$ model is simulated using a standard velocity-Verlet time integration with a timestep of 1 femtosecond. Periodic boundary conditions are applied in $x, y,$ and z directions in order to mimic a specimen with an infinite size. At the beginning of each simulation an energy minimization based on the conjugate gradients method is used on the initial nanoporous aluminum models. During the energy minimization process the boundaries of the nanoporous aluminum models are allowed to expand or contract freely. Afterwards a canonical ensemble NVT with a Nose-Hoover thermostat is performed for 25 picoseconds to thermally equilibrate the nanoporous aluminum. In order to mitigate the initial pre-stress in the nanoporous aluminum model, an isothermal-isobaric ensemble NPT is invoked for another 25 picoseconds.

Then after energy minimizations and equilibration we apply a tensile load to the nanoporous aluminum model, under an NVT ensemble, with a strain rate of $\frac{10^{-3}\%}{\text{ps}}$. The uniaxial, apparent stress was calculated based on virial stress as follows:

$$\sigma_{ij} = \frac{1}{V}\sum_{k\in V}\left(-m^{(k)}\left(u_i^{(k)} - \overline{u}_i\right)\left(u_j^{(k)} - \overline{u}_j\right) + \frac{1}{2}\sum_{l\in V}\left(x_i^{(l)} - x_i^{(k)}\right)f_j^{(kl)}\right) \qquad (3.4)$$

where N is the number of atoms in the system, k and l are atoms in the domain, V is the volume of the domain, $m^{(k)}$ is the mass of atom k, $u_i^{(k)}$is the i^{th} component of the velocity of atom k, $\overline{u}_j$ is the j^{th} component of the average velocity of the atoms in the volume, $x_i^{(k)}$ is the i^{th} component of the position of atom k, and $f_i^{(kl)}$ is the i^{th} component of the force applied on atom k by atom l. All the visualizations of the models are depicted using OVITO software.

3.3 Mechanism of Failure

To study how nanoporous aluminum fails during deformation multiple simulations have been performed to determine the dominating failure mechanism. A representative ligament is shown in Figure 3.2 to illustrate the deformation process of nanoporous aluminum.

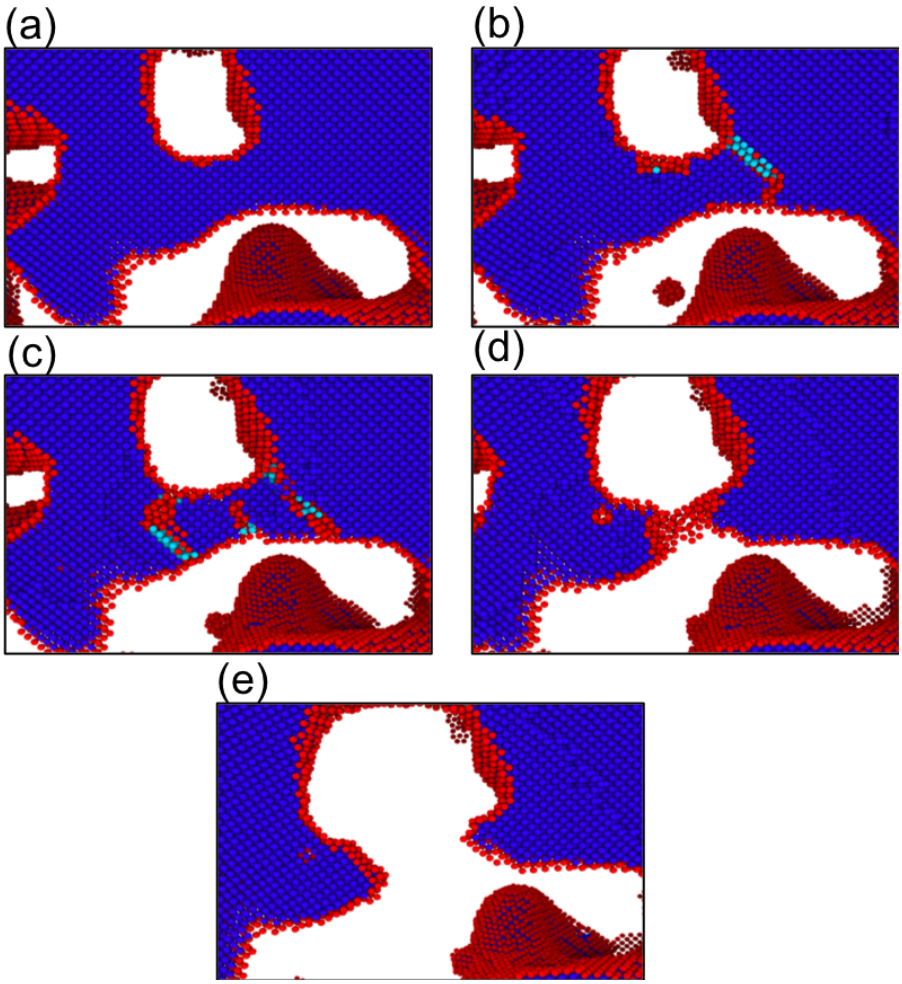

Figure 3. 2: Failure evolution of an np-Al ligament with cross-section view under the tensile loading: (a) the np-Al is unstrained; (b) strain causes a stacking fault in one ligament junction and a third dislocation is nucleating; (c) both junctions have formed dislocations and a third dislocation begins in the center of the ligament; (d) a lattice vacancy is produced as the two junction dislocations relax into FCC crystal when the ligament begins to neck; (e) complete failure occurs.

Dislocations in this chapter are defined by a common neighbor analysis calculation (CNA) which shows the packing arrangement of each atom. FCC aluminum is shown in blue, hexagonal close packed aluminum is shown in cyan, and disordered atoms are shown in red. When the CNA calculation undergoes a shift, which demarcates a change in packing arrangement, it is noted as a dislocation forming. It can be observed that dislocations nucleate at the surfaces of joints; at the surface because the high surface-energy lowers the stress needed to activate a dislocation, and at

the joints because torque generated during the tensile loading is largest in the ligament joints. As strain increases slip systems begin to develop in the thinnest segment of the stressed ligament followed by necking and rupture. The dislocation motifs seen in our nanoporous aluminum simulation include Lomer-Cottrell locks inside joints and parallel slip planes. Lomer-Cottrell locks are seen to develop in ligament junctions and cause dislocation pile-ups, which may help fracture resistance in the junctions by preventing further slippage between planes. Similar failure mechanisms, specifically dislocations initiating at the joints of ligaments, have been observed via MD studies for nanoporous gold. Load bearing ligaments, ligaments closely aligned with the loading direction, were observed to fail first and dominate the failure of nanoporous aluminum but for ligaments not aligned with the loading direction shearing was observed during plastic failure.

3.4 Young's Modulus

Two defining properties for the mechanical performance of nanoporous metals are chosen as the independent variables in this study: relative density and ligament diameter. We vary the relative density from 36% to 84%, using an average ligament diameter of 4.92 nm ± 0.34 nm, and then perform tensile simulations. For ligament diameter studies, we create models with average ligament diameters ranging from 3.11 nm to 9.88 nm, with a relative density of 41% ± 0.27%. In Figure 3.3 the stress-strain responses can be seen. For each curve the stress increases linearly at the beginning of tensile loading until about 95% of strain-at-failure, then the slope begins and continues to decrease for the last 5% until the failure strain is reached, at which point the slope inflects again becoming negative with a gradual slope denoting the necking of nanoporous aluminum ligaments before complete failure. Aside from these similarities the graphs show dissimilar trends which are the focus of the rest of this paper. Using calculations

from these stress-strain graphs we will share our findings concerning the mechanical properties and scaling laws of nanoporous aluminum and compare them to previous studies on open-cell metal foams.

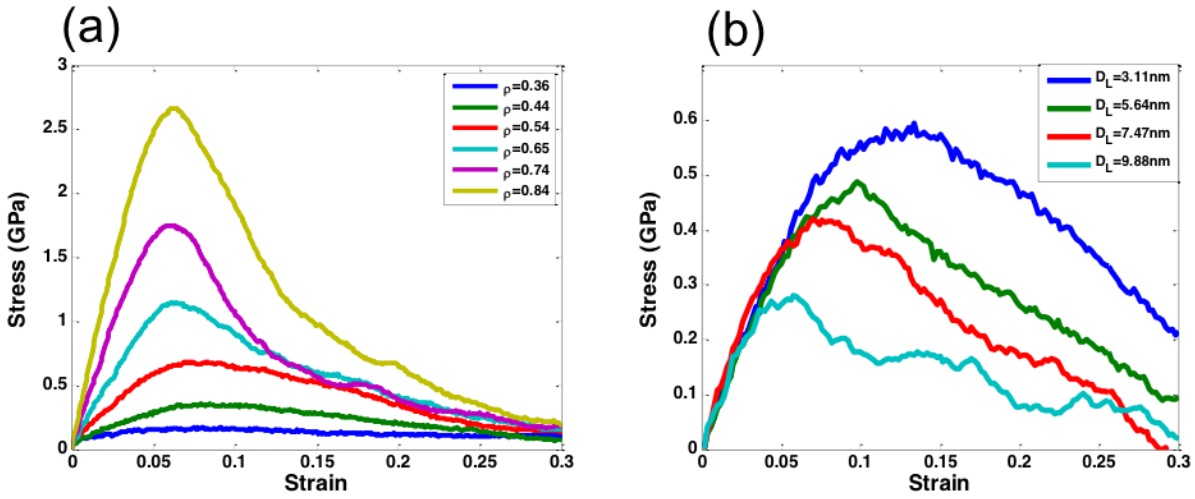

Figure 3. 3: Stress-strain relationships: (a) nanoporous aluminum models from Figure 3.1(b) with varying relative densities but the same average ligament diameter. (b) nanoporous aluminum models from Figure 3.1(c) with different ligament diameters but the same relative densities.

The first mechanical property of nanoporous aluminum to be discussed is the Young's modulus, taken as the line of best fit of stress-strain data from zero strain to 3% strain. The Young's modulus allows for determination of a material's stiffness at ordinary working conditions; that is at low strain under elastic deformation. It is observed in Figure 3.4(a) that decreasing the relative density lowered the Young's modulus, E, of the nanoporous aluminum following a cubic power-law relationship.

$$E = 82.96\rho^3 \tag{3.5}$$

Following the Ashby-Gibson's model which states that open-cell foams have a Young's modulus-relative density relationship of $E = C\rho^2$, the coefficient $C = 60.92$ for our simulation

data. From the regression analysis in Figure 3.4(a), it can be seen that the Young's modulus of nanoporous aluminum in the study does not scale as subtly as the Ashby-Gibson model predicts. Sun *et al*. also pointed out the discrepancy with the Ashby-Gibson scaling law for nanoporous gold and developed a scaling law better suited for predicting the Young's modulus of nanoporous gold with respect to relative density: $E = C_a(\rho^2 + C_b\rho)$. The attempt to fit Ashby and Gibson's scaling law and Sun's scaling law to our data is shown in Figure 3.4(a). The curve based on Sun's scaling law describes our simulation data well but at low relative densities, below 35%, it predicts a negative Young's modulus. This disparity stimulates us to propose the scaling law shown in Equation (3.5) which is similar to the Ashby-Gibson relationship for mesoscale foams but scaling cubically instead of quadratically. These findings exemplify the differences in mechanical properties between nanoscale, porous materials and mesoscale, porous materials, thereby offering new insights into the mechanical property behavior of nanoporous metals.

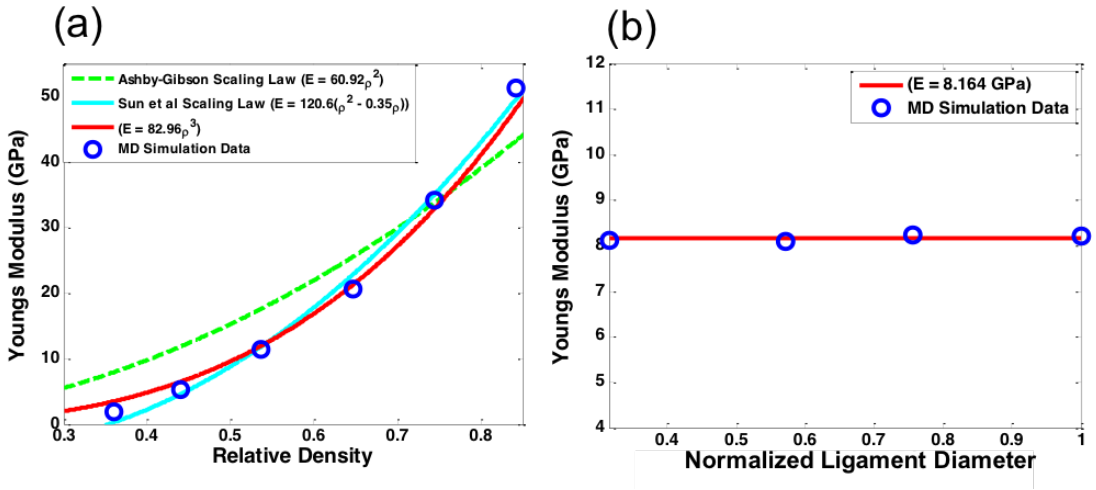

Figure 3. 4: (a) Young's modulus as a function of relative density along with three possible scaling laws to describe the molecular dynamics data. (b) Young's modulus versus ligament diameter; note that there is no perceptible change in Young's modulus.

Ligament size appears to have no effect on the Young's modulus, Figure 3.4(b), the Young's modulus remains, for all intents and purposes, constant when the average ligament

diameter of nanoporous aluminum is changed at constant relative density. When changing ligament diameter from 3.11 nm to 9.88 nm Young's modulus varies, with no trend, by less than 1% between the values of 8.1 and 8.2 GPa, a similar trend is evidenced by Sun *et al*. for nanoporous gold.

3.5 Yield Strength

Yield strength is a mechanical property that has been seen to be affected by both relative density and ligament size in previous literature. Figure 3.5(a) shows the yield strength calculated from molecular dynamics simulations of nanoporous aluminum plotted against relative density and is fit with three different scaling laws. It can be observed that the relative density has a dramatic effect on nanoporous aluminum's yield strength, with a 94% drop from 2.5 GPa to 0.16 GPa as the relative density decreases from 84% to 36%. Following the first Ashby-Gibson scaling law, $\sigma_s = C\rho$, describing the yield strength of open-cell foams that predominantly fail due to axial yielding of ligaments, we have fit the curve $\sigma_s = 1.821\rho$. According to another Ashby-Gibson scaling law, $\sigma_s = C\rho^{\frac{3}{2}}(1 + \rho^{\frac{1}{2}})$, describing the yield strength of open-cell foams that fail due to plastic collapse at junctions, we end up with a fitted curve $\sigma_s = 1.261\rho^{\frac{3}{2}}\left(1 + \rho^{\frac{1}{2}}\right)$. Neither scaling law closely fits the simulation data of yield strength versus relative density because, similar to the Young's modulus, the yield strength for nanoporous aluminum shows a stronger relationship to relative density than that which is predicted by classic Ashby-Gibson scaling laws. Ashby-Gibson scaling laws have been used to match the data for nanoporous gold, but here they fail to predict the change in yield strength of nanoporous aluminum. Therefore we propose a cubic scaling law,

$$\sigma_s = 3.771\rho^3 \tag{3.6}$$

which accurately matches our simulation data for the yield strength of nanoporous aluminum. Our scaling law supports the studies by Beiner *et al.*, Volkert *et al.*, and Hodge *et al.* who show that experimental values for yield strength are drastically different than those predicted by the Ashby-Gibson models and scale differently than the Ashby-Gibson scaling laws.

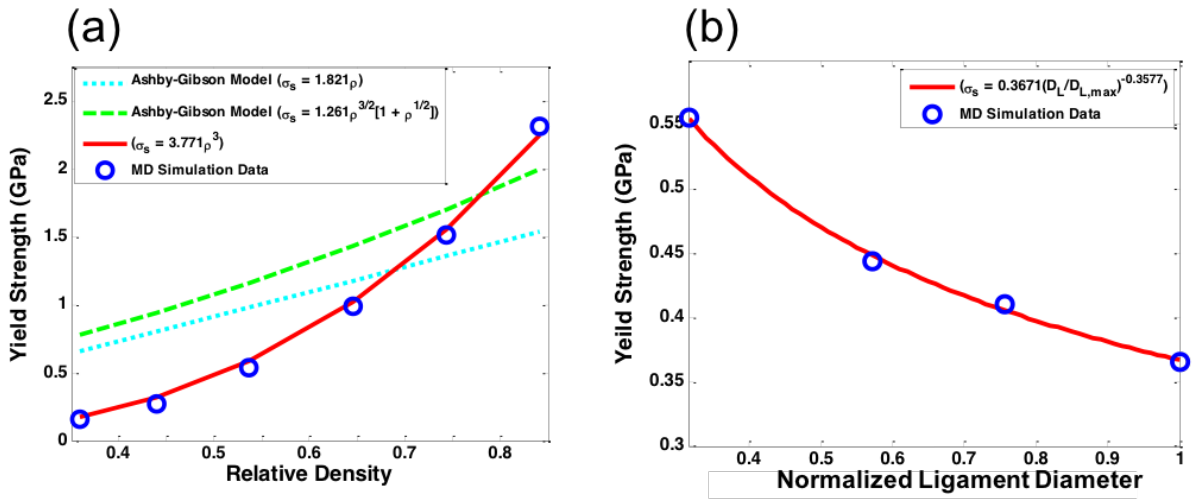

Figure 3. 5: (a) Yield strength as a function of relative density with two Ashby-Gibson scaling laws and a best fit curve fitted to the molecular dynamics data. (b) Yield strength as a function of normalized ligament diameter approaching an asymptote as the ligament diameter increases.

Volkert and Lilleodden show that yield strength is inversely proportional to ligament diameter in gold nanocolumns, $\sigma_s \propto D_L^{-n}$. Following this idea and using data in Figure 3.3(b), we find the same proportionality. The scaling law of the yield strength, when measured against the ligament size of nanoporous aluminum, is found to be:

$$\sigma_s = 0.3671 \left[\frac{D_L}{D_{L,max}}\right]^{-0.3577} \tag{3.7}$$

Here D_L is the ligament diameter and $D_{L,max} = 12.59nm$ is the largest average ligament diameter in our simulation models. Figure 3.5(b) shows a trend of increasing yield strength with

decreasing ligament size in nanoporous aluminum, which serves as support for the mantra that "smaller is stronger" in nanoporous metals. It seems relevant to point out that smaller ligaments creating stronger nanoporous structures is reminiscent of the well-known Hall-Petch relationship for grain size which parallels this finding by stating that yield strength is inversely proportional to grain size[33]. Of course these two phenomena describe two different mechanisms of increasing/decreasing a material's strength but the relationships, or scaling laws, are identical in form. These findings offer support for the fabrication of ever-smaller ligaments in nanoporous metals to provide devices, in harsh conditions, with the improved mechanical properties.

3.6 Ultimate Strength

Knowing the yield strength and ultimate strength of a material allows for more efficient implementation of metal forming processes that rely on lengthening, and allows for more reliable calculations when determining the failure of a material. Figure 3.6(a) shows the ultimate strength, σ_u, to relative density relationship, which again follows cubic power law:

$$\sigma_u = 4.337\rho^3 \tag{3.8}$$

Ultimate strength drastically decreases by 99% when relative density decreases from 84% to 36%.

Nanoporous aluminum's ultimate strength does not follow a similar scaling law as yield strength, or Young's modulus for that matter, with changes in ligament diameter. The relationship depicted in Figure 3.6(b) was best described as a linear function the relative ligament size as follows

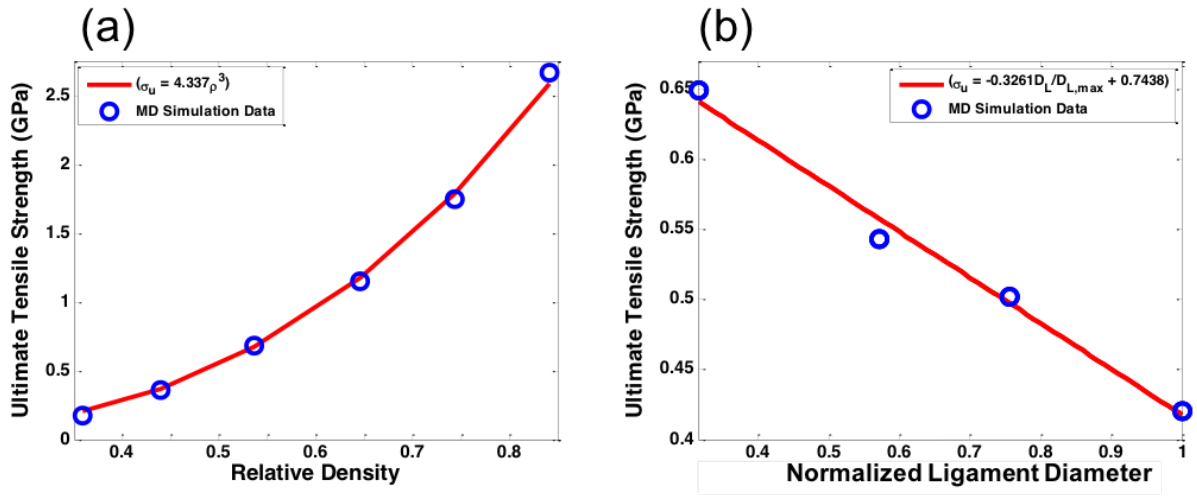

Figure 3. 6: (a) Ultimate tensile strength as a function of relative density. (b) Ultimate strength as a function of normalized ligament diameter. (c) Ultimate strength as a function of temperature.

$$\sigma_u = -0.33\frac{D_L}{D_{L,max}} + 0.7438. \tag{3.9}$$

It would be reasonable to say that this is a result of a small sample size because like yield strength, we initially predicted that ultimate strength would asymptotically approach a constant value as ligament diameter increased while ligament-size effects are not observed in meso/macro-porous materials.

3.7 Toughness

The toughness of a material is a useful metric which indicates the total amount of work which a material can absorb before it fails. Thus, knowing the toughness scaling law for nanoporous aluminum allows us to find suitable materials for energy/impact absorption. Toughness, K, is measured as the area under individual stress-strain curves until reaching ultimate strength. With respect to relative density, nanoporous aluminum's toughness decreases following the power law:

$$K = 170.3\rho^3 \tag{3.10}$$

and this relationship is plotted in Figure 3.7(a). Overall, the toughness of nanoporous aluminum drops by 90% from 105.85 $\frac{MJ}{m^3}$ to 10.68 $\frac{MJ}{m^3}$ across the range of relative density values. This is the lowest percentage drop among all the measured mechanical properties when relative density changes. Figure 3.8 shows an increase in strain until plastic deformation and failure. This phenomenon competes with the losses in toughness from reduction in material and dampens the effect of relative density on nanoporous aluminum's toughness.

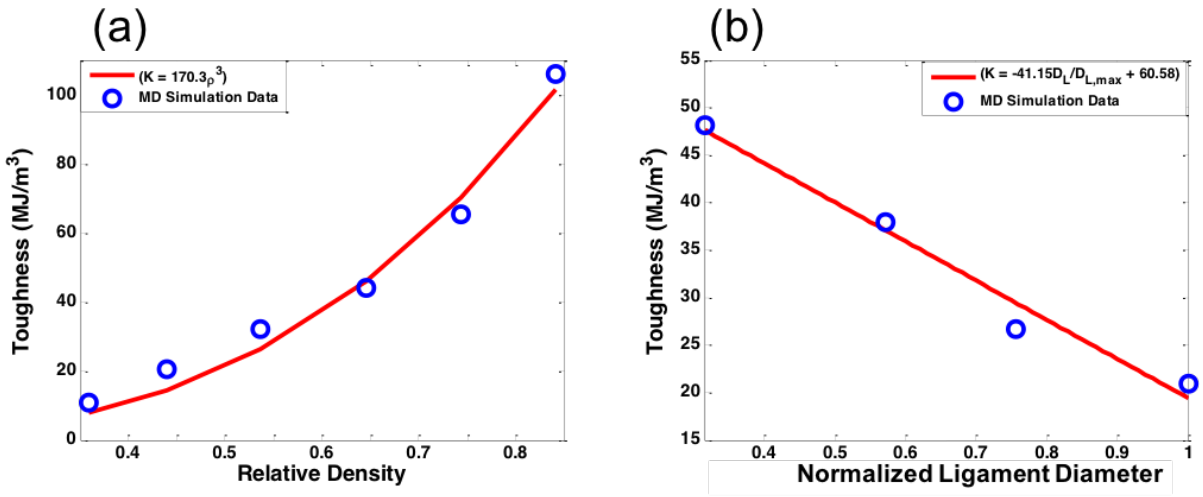

Figure 3. 7: (a) Toughness as a function of relative density. (b) Toughness as a function of normalized ligament diameter.

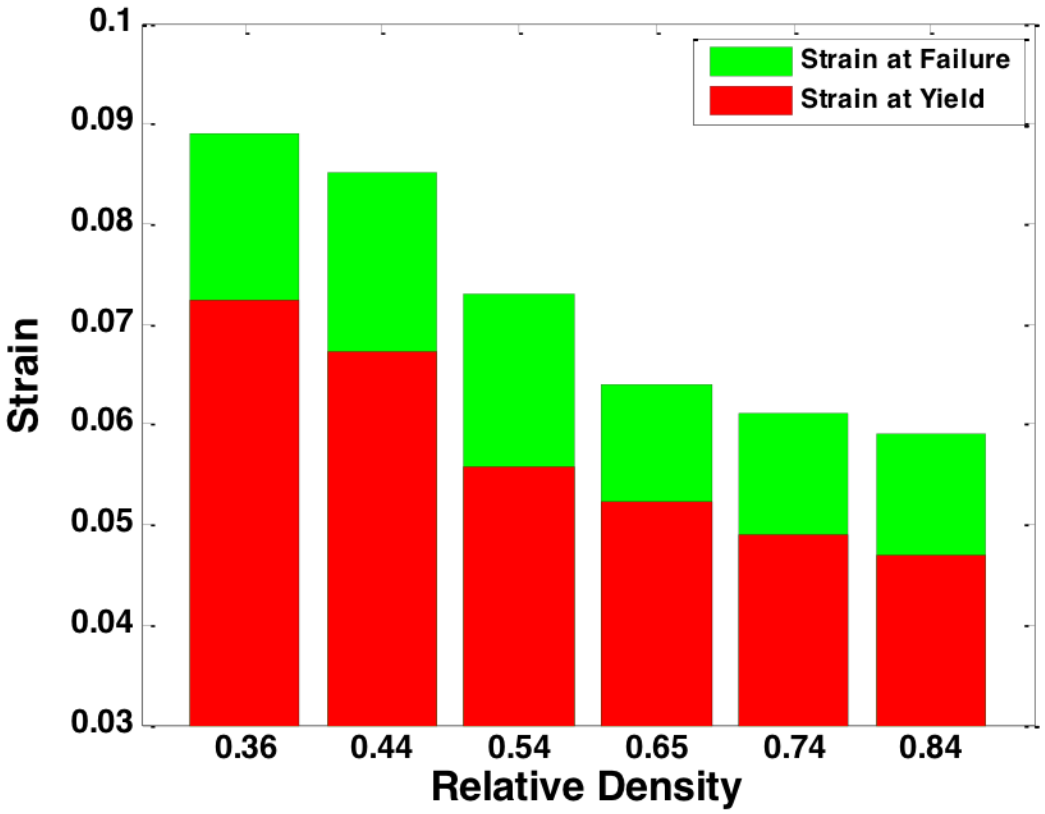

Figure 3. 8: Strain at failure and strain at yield for increasing relative density.

Toughness decreases by 56.5% as ligament diameter increases by 9.48 nm, a large drop in toughness for a change in diameter equivalent to only two FCC-aluminum-crystal unit cells. Decreasing the average ligament diameter, which increases the number of ligaments if relative density is constant, increases the energy needed to break the structure. Figure 3.7(b) shows the relationship:

$$K = -41.15\frac{D_L}{D_{L,max}} + 60.58 \tag{3.11}$$

which describes the effect of ligament size on nanoporous aluminum's toughness.

3.8 Chapter Summary

The tensile deformation behaviors and size effects of open-cell nanoporous aluminum were investigated using MD simulations. We conclude that dislocations in nanoporous aluminum originate at the surface of joints and shortly after in the thinnest section of the ligament causing necking and fracture. Lomer-Cottrell locks were frequently observed to form in the junctions between ligaments stopping further dislocations from forming in the junctions and encouraging dislocations in ligaments themselves. Relative density was found to play the most important role in affecting the mechanical properties of nanoporous aluminum when including ligament-size effects. Most importantly, a number of scaling laws were found for Young's modulus, yield stress, ultimate stress, and toughness of nanoporous aluminum. This study provides useful insights into the understanding of the fundamental mechanism and scaling laws of nanoporous materials.

CHAPTER 4 GENERATING STOCHASTIC, NON-OVERLAPPING FIBROUS NETWORKS FOR MATERIAL MODELLING

Fibrous materials are numerous and widely used - Plant fibers (cellulose and lignin), Animal fibers (collagen, silk, wool, sinew, etc.), Metallic fibers (aluminized nylon, aluminized plastic, gold, silver, etc.), Glass fibers (E-glass epoxy, S-glass epoxy, polyester resin, etc.), Polymer fibers (PET, PVC, PE, PU, etc.), and so on. In this chapter a method to generate stochastic fibrous network structures in periodic boxes is detailed and discussed. In the model, fiber length, diameter, curvature, and orientation are stochastically chosen using relevant probability density functions. Fibers are made to not overlap by integrating through the network iteratively considering contact forces between fibers, and fiber restoring forces in the context of beam theory. Key material properties of fibrous materials (mechanical, thermal, acoustic, electrical, and transport) are greatly influenced by the fiber material and the fibrous network structure (density, fiber length, fiber diameter, fiber orientation, and fiber curvature) which is, in general, stochastic. Creating a fibrous network model to investigate these materials computationally is a "packing problem" which have four classes soft-core, hard-core, non-deformable, and deformable. A soft-core model allows objects to overlap in the packed volume while hard-core models more realistically forbid the overlap of objects in the packed volume. Non-deformable models treat the objects being packed as rigid bodies, and deformable models allow for the deformation of objects either of which can be realistic depending on the objects being packed and the desired end result. For a fibrous network, where a fiber is loosely defined as an object with an aspect ratio of ~20 or greater with an arbitrary cross-section, the objects

should be hard-core and typically deformable. There have been several approaches to generate fibrous network structures that use different probability methods to generate fiber orientations, and fiber geometries, distinct fiber discretizations, and various methods for finding global/local equilibrium geometries. In general the lengths and diameters of the fibers are drawn from a gamma distribution.

Not all models control fiber orienation or are capable of controlling fiber orienation [73, 74]. The simplest selection method is to select orientations from a uniform distribution of random numbers between $-\pi$ and π which can be used when considering isotropic fibrous networks[75]. The most complex and most general orientation distributions involve orientation tensors and can be used to create a 3D probability density function for networks with multiple anisotropies[76]. However, the most prevelant probability model for stochastically controlling fiber orientations is the beta distribution [77, 78]. The beta distribution is an elegant single parameter, single variable function that may be used to generate isotropic network distributions or transverse isotropic network distributions. Though, the beta distribution allows for control of mean fiber orientation it does not allow for control of the dispersion of fiber orienations so we introduce a simple two parameter, single variable distribution function to control both the mean fiber orientation and the dispersion of the distribution to generate transverse isotropic and aligned networks.

Fiber geometry has had a variety of treatment in the past including fiber centerlines calculated by random walks filtered through a von Mises Fisher distrubution to step in a new random direciton, and centerlines that have been calculated using splines. The random walks with the von Mises Fisher distrubtion are based on a probability density function that allows for stochastic control over local curvature [79-82]. However, the von Mises Fisher random walk can produce unwanted features such as kinks depending on the step size and global curvature is not

directly controllable with this method. Splines have been used in the past with randomized tie/control points which lead to smooth fibers [80]. Here, a probability density method using Bezier splines is introduced to generate stochastic, smooth space curves with a controllable mean curvature and curvature dispersion as an alternative method to the von Mises Fisher random walk. Local fiber curvature then arises in the networks due to deformation while calculating equilibrium positions for fiber nodes.

Fiber discretization is perhaps the most widely varying subject in this area and is important for accurately calculating fiber-fiber contact, repulsion forces between fibers, and for code efficiency. Fibers have been descritized with a single ellipsoid, a single cylinder [83, 84], as a series of spheres [80], as a series of sphero-cylinders [80], as convex prisms capped by two dodecahedron [85], and so on. The discretization method is important and new methods can allow for greater computational efficiency or computational accuracy. The current model is a space-curve descritized by beams with contact forces calculated using Hertz contact theory. This descritization scheme is flexible and Hertz contact theory has been well studied.

In force biased approaches two forces need to be calculated for the fibers, forces between fibers due to contact/overlap and restoring forces within a fiber due to deformation. Beam theory is chosen to treat fiber displacement, rotation, and deformation since, given a series of discrete points along a space-curve, with the points being separated by a sufficiently large distance, a smooth continous deformation can still be obtained.

The methods are presented in the order that they would be implented in a computer code and pictorial representations of each method are shown and discussed.

4.1 Soft-Core Fiber Model

Before creating a non-overlapping network we create a network of fibers with given lengths, diameters, orientations, and mean-curvatures without considering whether they overlap or not. Then beam mechanics and contact mechanics are coupled to relax the overlapping segments.

Fiber diameter and fiber length can both be approximated by a gamma distribution with shape parameter, α, and rate parameter, β, which are related to the expectation values, d_{avg} and L_{avg}, and standard deviations, σ_d and σ_L. The average value and standard deviation for fiber diameter and fiber length can be large values or small values however the shape of the gamma distribution is usually similar so it must first be calculated and then the distribution can be scaled and shifted to match the desired values; d_{avg}, L_{avg}, σ_d and σ_L. The gamma distribution, $g(h, \alpha, \beta)$, with random variable, h, is:

$$g(h) = \frac{\beta^{\alpha}}{(\alpha-1)!} h^{\alpha-1} e^{-\beta h} \tag{4.1}$$

where h can either be replaced with fiber diameter d or fiber length L. The gamma distribution can be integrated to obtain the cumulative distribution function (CDF).

$$CDF = \int_0^{\infty} g(h)\, dh = 1 - \frac{\alpha \beta^{\alpha} h^{\alpha} \Gamma(\alpha, \beta h)}{\alpha! (\beta h)^{\alpha}} \tag{4.2}$$

where $\Gamma(\alpha, \beta h)$ is the incomplete gamma function. Then using CDF value's as the x-axis and values of the stochastic variable h as the y-axis, uniformly distributed numbers can be used as query points for interpolation to pull random numbers from the gamma distribution.

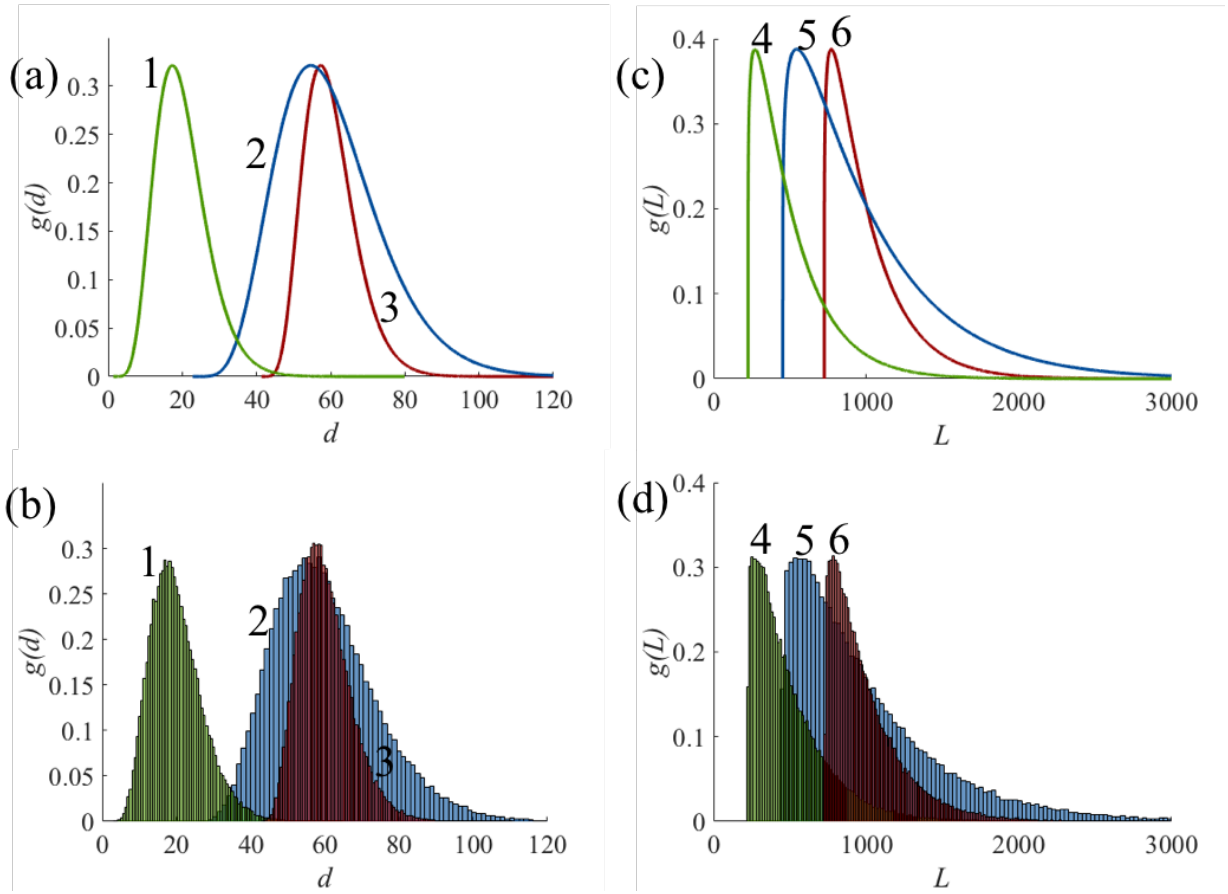

Figure 4. 1: (a) probability distributions for fiber diameters. (b) Histograms of 1000 fiber diameters randomly selected from the probability density functions: (1) $\alpha = 7$, $\beta = 2$, $d_{avg} = 60$, $\sigma_d = 7$ (2) $\alpha = 7$, $\beta = 2$, $d_{avg} = 60$, $\sigma_d = 14$ (3) $\alpha = 7$, $\beta = 2$, $d_{avg} = 20$, $\sigma_d = 7$. (c) probability distributions for fiber lengths. (d) Histograms of 1000 fiber lengths randomly selected from the probability density functions: (1) $\alpha = 1.2$, $\beta = 0.6$, $L_{avg} = 1000$, $\sigma_L = 250$ (2) $\alpha = 1.2$, $\beta = 0.6$, $L_{avg} = 1000$, $\sigma_L = 500$ (3) $\alpha = 1.2$, $\beta = 0.6$, $L_{avg} = 500$, $\sigma_d = 250$.

Fiber orientation, considering spherical coordinates, is a function azimuth, φ, and elevation, θ. For transverse isotropic networks azimuth angles are uniformly distributed and elevation angles are distributed with some mean, θ_{avg}, and some standard deviation, σ_θ. The beta distribution is successful in controlling mean fiber elevation but not the standard deviation of fiber elevation, Equation (4.3) is an altered version of an equation introduced by Fu and Lauke [86] which gives control of mean fiber elevation and standard deviation.

$$g(\theta) = \frac{\left[sin\left(\frac{\pi}{4}-\frac{\theta}{2}\right)^{2p-1}\right]\left[cos\left(\frac{\pi}{4}-\frac{\theta}{2}\right)^{2q-1}\right]+\left[sin\left(\frac{\pi}{4}-\frac{\theta}{2}\right)^{2q-1}\right]\left[cos\left(\frac{\pi}{4}-\frac{\theta}{2}\right)^{2p-1}\right]}{\int_{\theta_{min}}^{\theta_{max}}\left[sin\left(\frac{\pi}{4}-\frac{\theta}{2}\right)^{2p-1}\right]\left[cos\left(\frac{\pi}{4}-\frac{\theta}{2}\right)^{2q-1}\right]+\left[sin\left(\frac{\pi}{4}-\frac{\theta}{2}\right)^{2q-1}\right]\left[cos\left(\frac{\pi}{4}-\frac{\theta}{2}\right)^{2p-1}\right]d\theta} \quad (4.3)$$

The relationship in Equation (4.3) 5 has two parameters, p and q, and can represent a unimodal distribution or a bimodal distribution around zero. The integral of this distribution produces an equation involving the hypergeometric function which is not easily tractable and therefore prohibits us from finding analytic relationships between parameters, p and q, mean elevation, θ_{avg}, and standard deviation, σ_θ. To create an orientation distribution with a prescribed mean and standard deviation we store the orientation mean and standard deviation for all integer combinations of p and q between 1 and 1000 (Figure. 4.2). Then we input a desired mean and standard deviation and search the parameter spaces for the p/q combination that produces the closest match to the desired mean and standard deviation values.

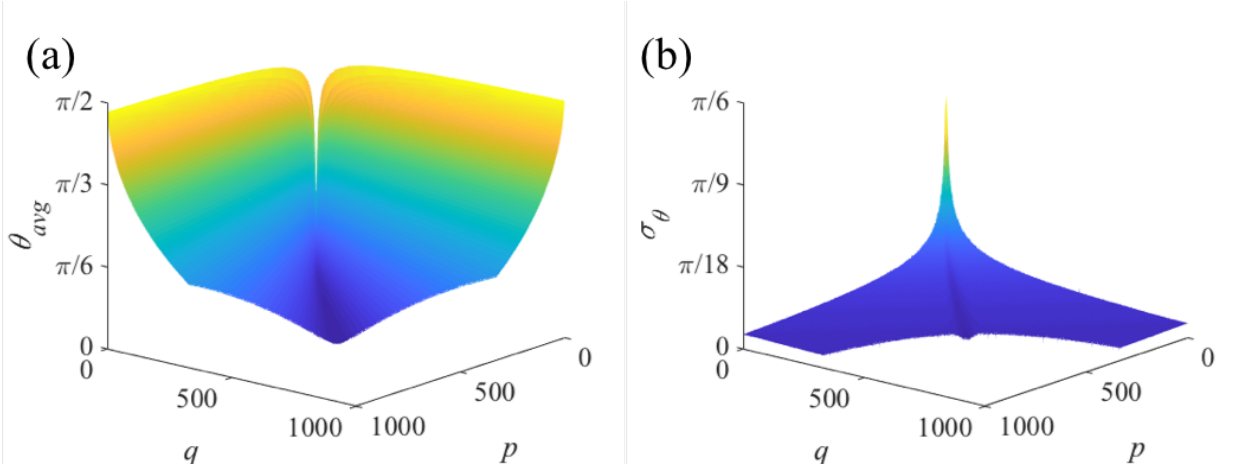

Figure 4. 2: (a) mean fiber orientation as a function of input parameters p and q. The surface is symmetric about the line $p = q$. The maximum mean elevation found for this surface between $p = 1$, $p = 1000$, $q = 1$, and $q = 1000$ was 87°, the minimum found was 1°. (b) fiber orientation standard deviation as a function of input parameters p and q. The surface is symmetric about the line $p = q$. The maximum standard deviation found for this surface between $p = 1$, $p = 1000$, $q = 1$, and $q = 1000$ was 23°, the minimum found was 1°. Only integer values were searched and the function may be searched for higher values of p and q.

$$CDF = \int g \, d\theta \tag{4.4}$$

Equation 4.4 is the CDF for the orientation distribution function, due to the complexity of the solution the CDF is solved for numerically using Simpson's method. Then using CDF value's as the x-axis and values of the stochastic variable θ as the y-axis, uniformly distributed numbers can be used as query points for interpolation to pull random numbers from the orientation distribution (Figure 4.3).

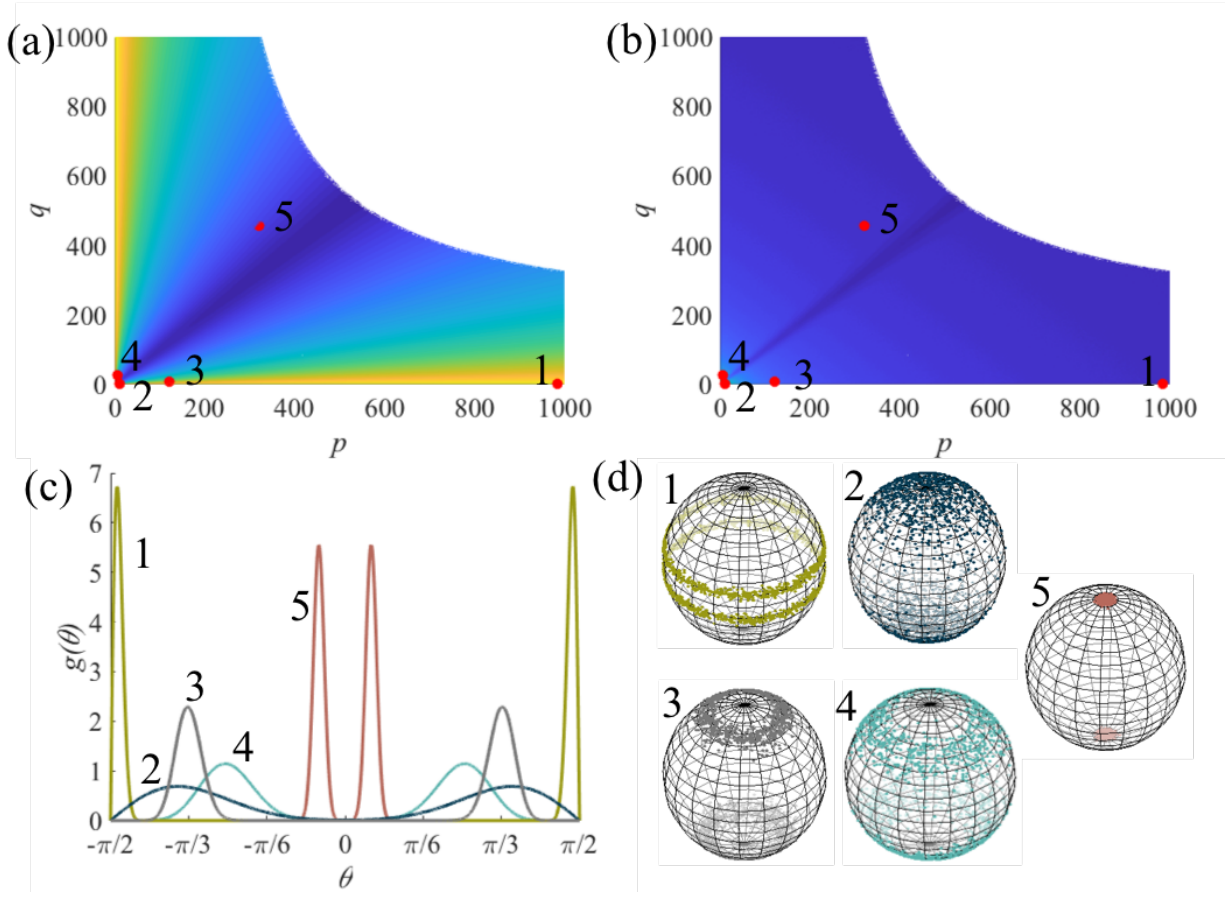

Figure 4. 3: Given 1000 fibers, a mean, and standard deviation five examples of the orientation distribution algorithm are represented and marked (1-5). In sub-Figures (a) and (b) points corresponding to p and q are selected from the mean and standard deviation surfaces. In sub-Figure (c) resulting probability density curves are plotted. In sub-Figure (d) the point at which each orientation vector

contacts the unit sphere is shown. (1) $\theta_{avg} = 85^{o}$, $\sigma_{\theta} = 1.5^{o}$ (2) $\theta_{avg} = 60^{o}$, $\sigma_{\theta} = 15^{o}$ (3) $\theta_{avg} = 60^{o}$, $\sigma_{\theta} = 5^{o}$ (4) $\theta_{avg} = 45^{o}$, $\sigma_{\theta} = 10^{o}$ (5) $\theta_{avg} = 10^{o}$, $\sigma_{\theta} = 2^{o}$

Fiber curvature is a unique topic in the stochastic structure of fibrous networks. Length and diameter are stochastic properties that have a single degree of freedom, there is only one way for a fiber to have a length of L, and assuming a circular cross-section there is only one way for a fiber to have a characteristic diameter of d. Fiber orientation has three degrees of freedom, however when considering a transverse isotropic or aligned network the degrees of freedom that need to be controlled are reduced to one. On the other hand there are infinitely many ways for a continuous curve to have a curvature, κ. In three dimensions each point along the curve has three degrees of freedom and each curve has, in principle, an infinite number of points. Here we let a space curve have 9 degrees of freedom, three degrees each for its endpoints, $\bar{P}_0$ and $\bar{P}_2$, and three for a control point, $\bar{P}_1$. Then those degrees of freedom are reduced to 3 by putting constraints on $\bar{P}_0$ and $\bar{P}_1$, and only letting $\bar{P}_2$ vary. In this case a formal definition for a fiber's center-line can be described by a quadratic Bezier curve parametrized by t in Equation (4.5) with first and second derivatives , Equations (4.6, 4.7), respectively.

$$\bar{C}(t) = \bar{P}_0(1-t)^2 + \bar{P}_1(1-t)t + \bar{P}_2 t^2 \tag{4.5}$$

$$\bar{C}'(t) = 2(1-t)(\bar{P}_1 - \bar{P}_0) + 2t(\bar{P}_2 - \bar{P}_1) \tag{4.6}$$

$$\bar{C}''(t) = 2(\bar{P}_2 - \overline{2P_1} + \bar{P}_0) \tag{4.7}$$

where the constraints are $\bar{P}_0 = \bar{s}_i$ ($\bar{s}_i$ being the seed point for fiber i) and $\bar{C}\left(t = \frac{1}{2}\right) = \frac{L_i \bar{\mu}_i}{2} + \bar{s}_i$. $\bar{s}_i$ is the seed point for fiber *i*, L_i is the length of fiber *i*, and μ_i is the orientation vector of fiber *i.* The second constraint indirectly constrains the control point $\bar{P}_1$. The next step is to consider that the last point needed to fully define $\bar{C}(t)$ for fiber i may be any point that is approximately a distance of $\frac{L_i}{2}$ away from $\bar{C}\left(t = \frac{1}{2}\right)$ and can therefore be constrained to a sphere. The search for $\bar{P}_2$ can be further reduced to an arc, $\breve{A}$, along the sphere centered at $\bar{C}\left(t = \frac{1}{2}\right)$ with a radius $\frac{L_i}{2}$ which includes the trivial case of $\bar{P}_0$, $\bar{C}\left(t = \frac{1}{2}\right)$, and $\bar{P}_2$ lying on a straight line (pictured in Figure 4.4). Then the curvature (Equation (4.8)) of a Bezier curve can be calculated and assigned a probability value from the Gaussian distribution (Equation (4.9)). Through a specific point a Bezier curve can be selected from a probability distribution function given a mean curvature and standard deviation, κ_{avg} and σ_κ.

$$\kappa = \frac{1}{m}\sum_1^m \frac{\left\|\bar{C}'(t)\times\bar{C}''(t)\right\|}{\|\bar{C}'(t)\|^3} \tag{4.8}$$

$$g(\kappa) = \frac{1}{\sqrt{2\pi\sigma_\kappa^2}} e^{-\frac{(\kappa-\kappa_{avg})^2}{2\sigma_\kappa^2}} \tag{4.9}$$

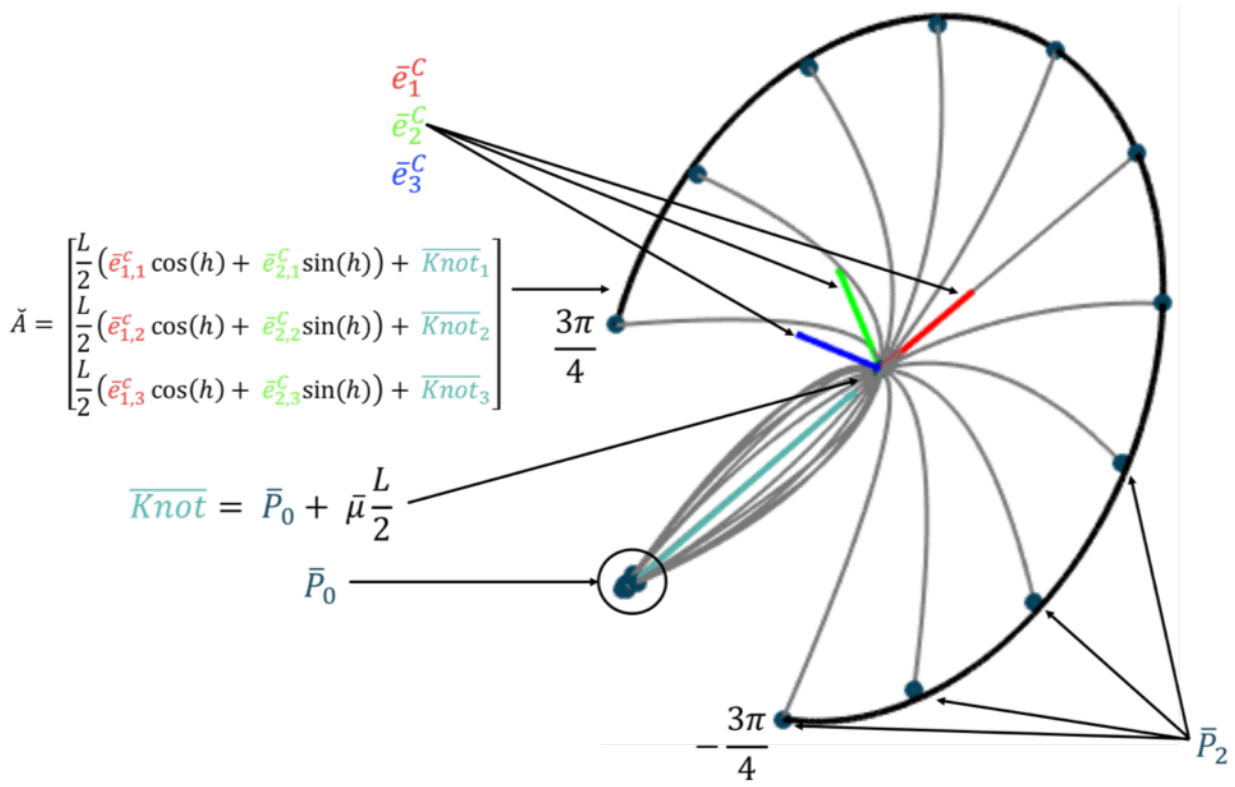

Figure 4. 4: A pictorial representation of the geometry involved in generating Bezier splines along an arc. (Tie point $\bar{P}_0$ is seen to change even though its position was initially a constrained point when drawing the Bezier splines. This is done after the spline selection process, ends are cut to preserver the initial length of the fiber).

At the is point, the spline selection is carried out in a similar fashion to select fiber diameters, lengths, and orientations by integrating the probability distribution function (Equation (4.9)) and using the result in combination with uniformly generated numbers and linear interpolation to pull randomly from the distribution (Figure 4.5).

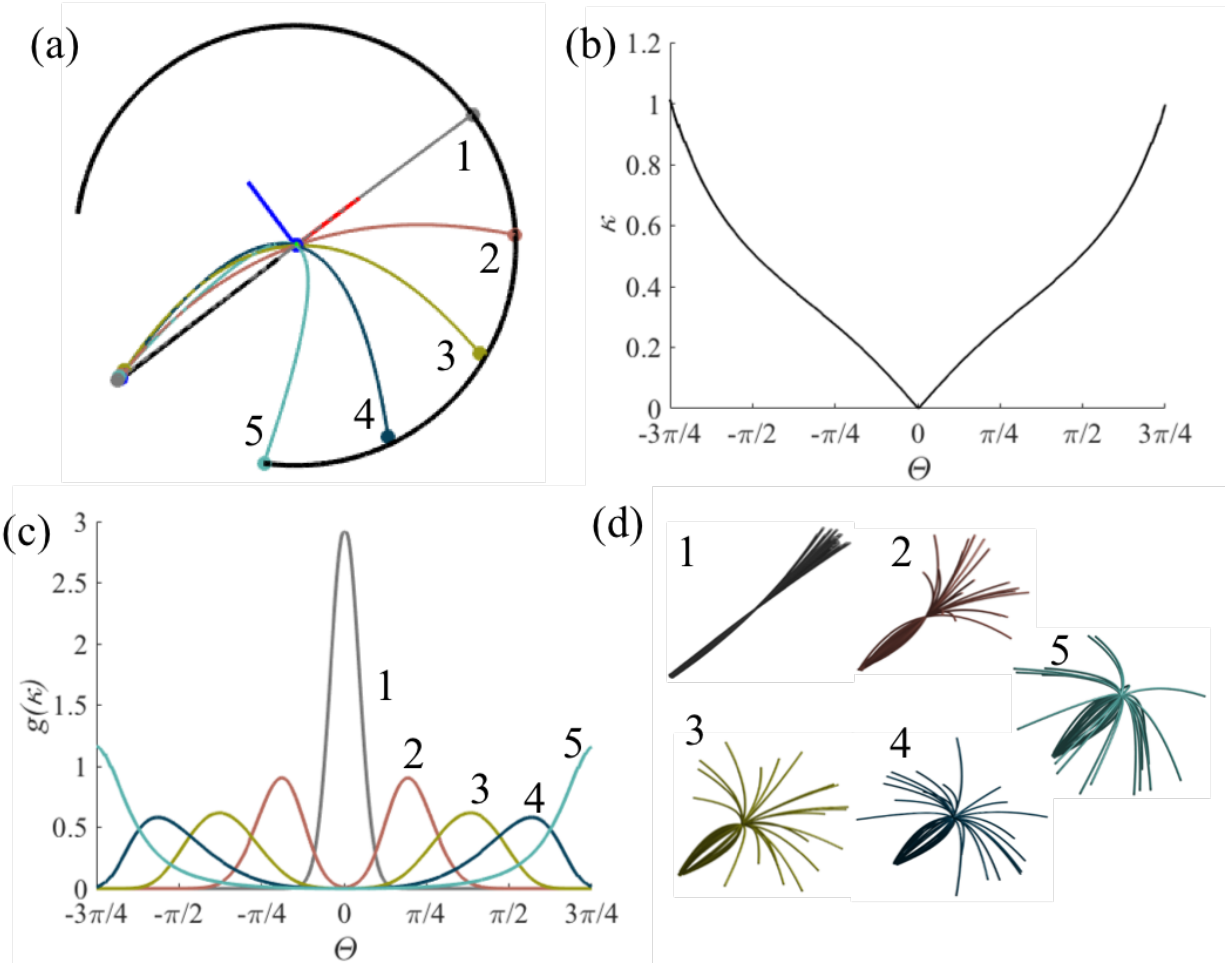

Figure 4. 5: (a) Average space curve for five different κ_{avg} and σ_{κ} values using quadratic Bezier curves that are 5 length units long: (1) $\kappa_{avg} = 0.0036$, $\sigma_{\kappa} = 0.05$ (2) $\kappa_{avg} = 0.22$, $\sigma_{\kappa} = 0.07$ (3) $\kappa_{avg} = 0.39$, $\sigma_{\kappa} = 0.10$ (4) $\kappa_{avg} = 0.59$, $\sigma_{\kappa} = 0.15$ (5) $\kappa_{avg} = 1.01$, $\sigma_{\kappa} = 0.25$. (b) Curvature as a function of rotating $\bar{P}_2$ along the arc $\breve{A}$. (c) Probability density curves for the five different cases when assigning the position of $\bar{P}_2$ moving along the arc $\breve{A}$ a probability using the gaussian distribution function. (d) Representative fiber bundles for each probability density curve where each fiber has the same seed position, length, and orientation.

Putting it all together and making slight modifications for specific fibrous network geometries soft-core network models can be created with stochastic fiber diameters, lengths, orientations, and curvatures. Certain geometries of interest are dense isotropic networks with fiber orientations distributed about a plane such as in paper materials, aligned fiber networks

such as carbon-nanotube forests, and sparse networks with inclusions such as blood clots (Figure 4.6).

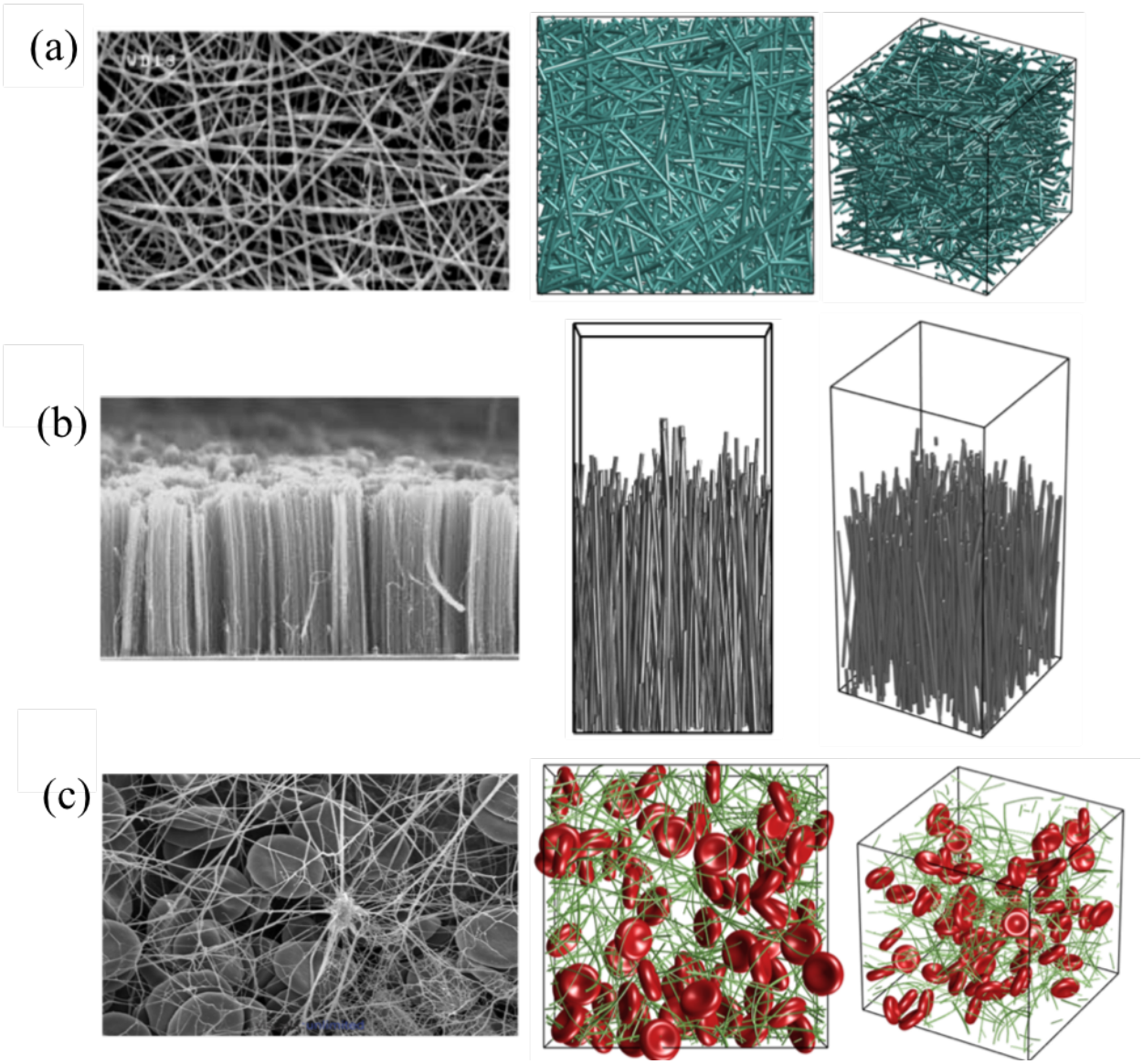

Figure 4. 6: Soft core models using algorithms 1 through 3 including slight variations. Row (a) bacterial nanocellulose mat. (b) Single-walled carbon nanotube forest, seed positions are assigned random x and y coordinates with 0 as the z-coordinate value and the z-value of the simulation box is increased. (c) Fibrin and blood cells forming a blood clot, blood cells are added as inclusions in the network.

4.2 Hard-Core Fiber Model

First-order, shear-deformable, Timoshenko beam theory models the continuous deformation of a beam subjected to normal forces, shear forces, and moments. Transverse shear strain is considered to be constant through the beam's cross-section and so cross-sections remain undistorted after deformation however they do not necessarily remain normal to the longitudinal axis after deformation. Each beam has two nodes (i, j) and each node has three translational (u_x, u_y, u_z) and three rotational $(\theta_x, \theta_y, \theta_z)$ degrees of freedom. A full derivation for force displacement relations can be found from Luo [87], a summary and necessary equations will be given here as well as a derivation of the energy-displacement relations and its derivatives. Energy-displacement relationships are required to perform energy minimization of the soft-core system to the hard-core system.

Displacements and rotations calculated in the local reference frame for the beam have a '-superscript and those rotated into the global frame drop the superscript. All relationships are considered to vary along the central axis of the beam, x'_x, and are considered to be constant in directions perpendicular to the beams central axis, x'_y and x'_z. Displacement along the axial direction, u'_x, and rotation around the axial direction, θ'_x, are considered to be linear functions of x'_x, where x'_x ranges from 0 to l.

$$u'_x = a_0 + a_1 x'_x \tag{4.10}$$

$$\theta'_x = d_0 + d_1 x'_x \tag{4.11}$$

Displacement in the y and z-directions, u'_y and u'_z, are considered to be cubic functions and rotations around the y and z-axes are related to the derivatives of the displacements, θ'_y and θ'_z.

$$u_y' = b_0 + b_1 x_x' + b_2 x_x'^2 + b_3 x_x'^3 \tag{4.12}$$

$$\theta_z' = \frac{du_y'}{dx_x'} - \gamma_{xy} = b_1 + 2b_2 x_x' + 3b_3 x_x'^2 + \frac{6EI}{\kappa GA} b_3 \tag{4.13}$$

$$u_z' = c_0 + c_1 x_x' + c_2 x_x'^2 + c_3 x_x'^3 \tag{4.14}$$

$$\theta_y' = -\frac{du_z'}{dx_x'} + \gamma_{xy} = -c_1 - 2c_2 x_x' - 3c_3 x_x'^2 + \frac{6EI}{\kappa GA} c_3 \tag{4.15}$$

Where E is the elastic modulus, G is the shear modulus, A is the cross-sectional area, κ is the shear deflection constant, and for a beam with circular cross-section $I_{yy} = I_{zz} = I$ is the moment of inertia. Solving the system of equations with boundary conditions, equations 4.16, at the beams ends yields solutions for constants, equations 4.17, in equations 4.10 through 4.15.

$$\begin{cases} u_x'(0) = u_x'^{(1)}, u_y'(0) = u_y'^{(1)}, u_z'(0) = u_z'^{(1)}, \theta_x'(0) = \theta_x'^{(1)}, \theta_y'(0) = \theta_y'^{(1)}, \theta_z'(0) = \theta_z'^{(1)} \\ u_x'(l) = u_x'^{(2)}, u_y'(l) = u_y'^{(2)}, u_z'(l) = u_z'^{(2)}, \theta_x'(l) = \theta_x'^{(2)}, \theta_y'(l) = \theta_y'^{(2)}, \theta_z'(l) = \theta_z'^{(2)} \end{cases} \tag{4.16}$$

$$\begin{cases} a_0 = u_x'^{(1)}, a_1 = \frac{u_x'^{(2)} - u_x'^{(1)}}{l} \\ b_0 = u_y'^{(1)},\ b_1 = \frac{2\Phi\left(u_y'^{(2)} - u_y'^{(1)}\right) + \left(l^3 + \Phi l\right)\theta_z'^{(1)} - \Phi l \theta_z'^{(2)}}{l\left(l^2 + 2\Phi\right)} \\ b_2 = \frac{\Phi\left(\theta_z'^{(2)} - \theta_z'^{(1)}\right) + 3l\left(u_y'^{(2)} - u_y'^{(1)}\right) - l^2\left(\theta_z'^{(2)} + \theta_z'^{(1)}\right)}{l\left(l^2 + 2\Phi\right)}, b_3 = \frac{2\left(u_y'^{(1)} - u_y'^{(2)}\right) + \left(\theta_z'^{(2)} + \theta_z'^{(1)}\right)}{l\left(l^2 + 2\Phi\right)} \\ c_0 = u_z'^{(1)},\ c_1 = \frac{2\Phi\left(u_z'^{(2)} - u_z'^{(1)}\right) + \left(l^3 - \Phi l\right)\theta_y'^{(1)} - \Phi l \theta_y'^{(2)}}{l\left(2\Phi - l^2\right)} \\ c_2 = \frac{\Phi\left(\theta_y'^{(1)} - \theta_y'^{(2)}\right) + 3l\left(u_z'^{(1)} - u_z'^{(2)}\right) - l^2\left(\theta_y'^{(2)} + \theta_y'^{(1)}\right)}{l\left(2\Phi - l^2\right)}, c_3 = \frac{2\left(u_z'^{(2)} - u_z'^{(1)}\right) + l\left(\theta_y'^{(2)} + \theta_y'^{(1)}\right)}{l\left(2\Phi - l^2\right)} \\ d_0 = \theta_x'^{(1)}, d_1 = \frac{\theta_x'^{(2)} - \theta_x'^{(1)}}{l} \end{cases} \tag{4.17}$$

$$\Phi = \frac{6EI}{\kappa GA}, \kappa = \frac{10}{9} \text{ for a beam with a circular cross} - \text{section}$$

Then using the displacement functions, the linear definition of strain (eqn. 4.18), and the isotropic definition of stress (eqn. 4.19) the stress-strain relationships are derived (eqns. 4.20 and 4.21).

$$\varepsilon_{ij} = \frac{1}{2}\left(\frac{\partial u_i}{\partial x_j} + \frac{\partial u_j}{\partial x_i}\right) \tag{4.18}$$

$$\sigma_{ij} = \frac{E}{\nu+1}\left(\varepsilon_{ij} + \frac{\nu}{1-2\nu}\varepsilon_{kk}\delta_{ij}\right) \tag{4.19}$$

With ε_{ij} being strain, σ_{ij} being stress, δ_{ij} the kronecker delta, and ν the poisson's ratio.

$$\begin{cases} \varepsilon_{xx} = a_1 \\ \varepsilon_{xy} = \frac{3b_3x_x'}{2} + b_2 + \frac{1}{2}b_1 \\ \varepsilon_{xz} = \frac{3c_3x_x'}{2} + c_2 + \frac{1}{2}c_1 \\ \varepsilon_{yy} = \varepsilon_{zz} = \varepsilon_{yz} = 0 \end{cases} \tag{4.20}$$

$$\begin{cases} \sigma_{xx} = \frac{E\left(a_1 + \frac{a_1\nu}{\nu+1}\right)}{\nu+1} \\ \sigma_{yy} = \sigma_{zz} = \frac{E\nu a_1}{(\nu+1)^2} \\ \sigma_{xy} = \frac{E\left(\frac{3b_3x_x'}{2} + b_2 + \frac{1}{2}b_1\right)}{\nu+1} \\ \sigma_{xz} = \frac{E\left(\frac{3c_3x_x'}{2} + c_2 + \frac{1}{2}c_1\right)}{\nu+1} \\ \sigma_{yz} = 0 \end{cases} \tag{4.21}$$

From the definition of strain-energy, $U = \int \sigma_{ij}\varepsilon_{ij}dV$ where U is the strain-energy and dV is the infinitesimal volume, strain-energy and its first partial derivatives can be calculated. Here the volume is that of a cylinder.

$$U = \frac{Elr^2\pi\left(15b_1^2+30b_1b_2l+30b_1b_3l^2+20b_2^2l^2+45b_2b_3l^3+27b_3^2l^4\right)}{60(\nu+1)} +$$

$$\frac{Elr^2\pi\left(15c_1^2+30c_1c_2l+30c_1c_3l^2+20c_2^2l^2+45c_2c_3l^3+27c_3^2l^4\right)}{60(\nu+1)} + \frac{Ea_1^2lr^2\pi(2\nu+1)}{2(\nu+1)^2} \tag{4.22}$$

$$\begin{cases}
\dfrac{\partial U}{\partial u_x'^{(1)}} = \dfrac{Er^2\pi\left(2u_x'^{(1)}-2u_x'^{(2)}\right)(2\nu+1)}{2l(\nu+1)^2} \\
\dfrac{\partial U}{\partial u_y'^{(1)}} = \dfrac{Er^2\pi\left[\left(120\Phi^2+36l^4+120\Phi l^2\right)\left(u_y'^{(1)}-u_y'^{(2)}\right)+3l^5\left(\theta_z'^{(1)}+\theta_z'^{(2)}\right)\right]}{60l(\nu+1)(l^2+2\Phi)^2} \\
\dfrac{\partial U}{\partial u_z'^{(1)}} = -\dfrac{Er^2\pi\left[\left(120\Phi^2+36l^4-120\Phi l^2\right)\left(u_z'^{(1)}-u_z'^{(2)}\right)+3l^5\left(\theta_y'^{(1)}+\theta_y'^{(2)}\right)\right]}{60l(\nu+1)(2\Phi-l^2)^2} \\
\dfrac{\partial U}{\partial \theta_x'^{(1)}} = 0 \\
\dfrac{\partial U}{\partial \theta_y'^{(1)}} = \dfrac{Er^2\pi\left[\left(10\Phi^2l^2-10\Phi l^4\right)\left(\theta_y'^{(1)}-\theta_y'^{(2)}\right)+l^6\left(4\theta_y'^{(1)}-\theta_y'^{(2)}\right)+3l^5\left(u_z'^{(2)}-u_z'^{(1)}\right)\right]}{60l(\nu+1)(2\Phi-l^2)^2} \\
\dfrac{\partial U}{\partial \theta_z'^{(1)}} = \dfrac{Er^2\pi\left[\left(10\Phi^2l^2+10\Phi l^4\right)\left(\theta_z'^{(1)}-\theta_z'^{(2)}\right)+l^6\left(4\theta_z'^{(1)}-\theta_z'^{(2)}\right)+3l^5\left(u_y'^{(1)}-u_y'^{(2)}\right)\right]}{60l(\nu+1)(2\Phi+l^2)^2} \\
\dfrac{\partial U}{\partial u_x'^{(2)}} = -\dfrac{Er^2\pi\left(2u_x'^{(1)}-2u_x'^{(2)}\right)(2\nu+1)}{2l(\nu+1)^2} \\
\dfrac{\partial U}{\partial u_y'^{(2)}} = -\dfrac{Er^2\pi\left[\left(120\Phi^2+36l^4+120\Phi l^2\right)\left(u_y'^{(1)}-u_y'^{(2)}\right)+3l^5\left(\theta_z'^{(1)}+\theta_z'^{(2)}\right)\right]}{60l(\nu+1)(l^2+2\Phi)^2} \\
\dfrac{\partial U}{\partial u_z'^{(2)}} = \dfrac{Er^2\pi\left[\left(120\Phi^2+36l^4-120\Phi l^2\right)\left(u_z'^{(1)}-u_z'^{(2)}\right)+3l^5\left(\theta_y'^{(1)}+\theta_y'^{(2)}\right)\right]}{60l(\nu+1)(2\Phi-l^2)^2} \\
\dfrac{\partial U}{\partial \theta_x'^{(2)}} = 0 \\
\dfrac{\partial U}{\partial \theta_y'^{(2)}} = \dfrac{Er^2\pi\left[\left(10\Phi^2l^2-10\Phi l^4\right)\left(\theta_y'^{(1)}-\theta_y'^{(2)}\right)+l^6\left(4\theta_y'^{(2)}-\theta_y'^{(1)}\right)+3l^5\left(u_z'^{(1)}-u_z'^{(2)}\right)\right]}{60l(\nu+1)(2\Phi-l^2)^2} \\
\dfrac{\partial U}{\partial \theta_z'^{(2)}} = -\dfrac{Er^2\pi\left[\left(10\Phi^2l^2+10\Phi l^4\right)\left(\theta_z'^{(1)}-\theta_z'^{(2)}\right)+l^6\left(\theta_z'^{(1)}-4\theta_z'^{(2)}\right)+3l^5\left(u_y'^{(2)}-u_y'^{(1)}\right)\right]}{60l(\nu+1)(2\Phi+l^2)^2}
\end{cases} \tag{4.23}$$

4.3 Discussion

Chapter 4 ends here with a discussion of the current progress and future plans. The current addition needed to move the soft-core fiber networks to a hard-core fiber network configuration is a solution to the contact problem between two beams. This is needed for

minimizing the energy of the system. This work is still on going and is being solved within the framework of Hertzian contact theory. To summarize the chapter a number of statistical models have been used to capture the geometry of fibrous networks so that they may be generated as computer models. These statistical models include the gamma distribution to capture the stochastic distribution of fiber lengths and fiber diameters, a two-parameter sine-cosine distribution to model the orientations of fibers, and a Gaussian distribution generate fibers with a stochastic mean curvature. In Section 4.2 a derivation for the change in strain-energy of a beam as a function of the displacements and rotations at its two ends was given. These equations as well as the equations currently being derived for the change in strain-energy of a beam upon contact with another beam will be used in future work for energy minimization of the soft-core system to achieve a hard-core system. It is our intention to continue the work we performed for nanoporous materials with investigations into nanofibers including nanocellulose fibers and high-performance polymeric fibers used in fabric armors. The model is useful for generating a number of network configurations at any scale and so we also plan to use it for computationally investigating interactions between blood-clots, nanoparticles, and blood cells within capillaries.

CHAPTER 5 SUMMARY AND FUTURE PLANS

This work looked at the interplay of material geometry and mechanics with a focus in the computational modelling of nanomaterials and their reaction to mechanical loading. The studies were carried out using in-house code based on Euclidean geometry, phase-field PDE solvers, probability distributions, beam theory, and contact theory for generating material geometries and the open-source molecular dynamics package LAMMPS to simulate mechanical loading.

Our simulations in Chapter 2 and 3 show that the scaling laws of nanoporous silicon and nanoporous aluminum are dependent on pore geometry, relative density, and ligament thickness. Decreasing relative density results in decreases in all mechanical properties. Young's modulus for nanoporous silicon scaled as $E \propto \rho^n$ with n ranging from an almost stretching-dominated signature of 1.5 to a stochastic signature of 2.5, strength scaled as $\sigma_u \propto \rho^n$ with n ranging from 1.5 to 2, and toughness scaled as $\kappa \propto \rho^n$ with n ranging from 1.5 to 2.6. While Young's modulus for nanoporous aluminum scaled as $E \propto \rho^n$ with n equal to 3, strength scaled as $\sigma_u \propto \rho^n$ with n equal to 3, and toughness scaled as $\kappa \propto \rho^n$ with n equal to 3. Toughness in nanoporous silcon was found to be uncoupled from Young's modulus and strength such that a stronger, stiffer model may not be tougher than its weaker, less stiff counterpart. No decoupling was observed in nanoporous aluminum. Ligament thickness played a negligible effect on the Young's modulus of both nanoporous silicon and nanoporous aluminum. Size effects were not consistent for nanoporous silicon models with different nanostructures: nanoporous silicon with staggered circular pores and vertical elliptical pores became stronger and more ductile as ligament thickness decreased while nanoporous silicon with horizontal elliptical pores became

weaker as ligament thickness decreased and showed no discernable change in ductility as ligament thickness changed. The yield strength of both nanoporous silicon and nanoporous aluminum scaled inversely proportional to ligament thickness. Over the range of simulation data the yield strength of nanoporous silicon appeared to scale inversely and linear with ligament thickness and the yield strength of nanoporous aluminum scaled as $\sigma_y \propto d^{-n}$ with n equal 0.36. Nanostructure was seen to shape the stress distribution in nanoporous silicon and starve dislocations in nanoporous aluminum leading to changes in mechanical properties and material failure.

The work in Chapter 4 concluded a newly-developed method for creating soft-core fibrous network geometries with stochastic control of fiber lengths, diameters, orientations, and curvatures. These methods heavily rely on randomly selecting variables from non-uniform probability distributions and curvature selection included a simple Bezier spline method as well. A method for creating hard-core networks from the soft-core models was partially detailed and derivations for the necessary energy/displacement and energy-gradient/displacement equations in the framework of beam theory were shown. Together with contact energy formulas and an energy minimization algorithm the systems may be relaxed to non-penetrating configuration.

During this master's degree I have developed skills and continue to develop skills for modelling materials with complex geometries and simulating these models under mechanical loadings. In the future I wish to continue this work and become a professional within the mechanical materials community. That said I will outline future investigations. The size-effect problem is still a big issue in this field as it effects scaling laws, intrinsic mechanical properties, and plastic deformation. The theories of nanoscale elasticity and plasticity are currently being developed but several desires for these theories are already known. Those are that the theory is indiscriminate to types of materials (brittle, elastic, crystalline, amorphous, etc.) and the theory

returns the solutions of well-known elasticity and plasticity theories when the scale over a critical size (somewhere in the nano/micro-scale range). This creates three objectives for my future work as a computational investigator. One the ability to model the nano/micro-scale geometries and physics of brittle, elastic, crystalline, and amorphous materials in which size-effects present themselves, two to further my knowledge of classical and recent theories of elasticity and plasticity, and three improve my understanding of statistical techniques used to analyze data.

REFERENCES

1. Williams, E., *Some observations of Leonardo, Galileo, Mariotte and others relative to size effect.* Annals of Science, 1957. **13**(1): p. 23-29.
2. Galilei, G., *Discorsi e dimostrazioni matematiche*. 2013: Elsevier.
3. Mariotte, E., *Traité du mouvement des eaux et des autres corps fluides*. 1718: C.-Jombert.
4. Griffith, A.A. and M. Eng, *VI. The phenomena of rupture and flow in solids.* Phil. Trans. R. Soc. Lond. A, 1921. **221**(582-593): p. 163-198.
5. Midgley, E. and F. Pierce, *Tensile Tests for Cotton Yams, Part III: The Rate of Loading.* Journal of Textile Institute, 1926. **17**: p. T330-T341.
6. Tippett, L.H., *On the extreme individuals and the range of samples taken from a normal population.* Biometrika, 1925: p. 364-387.
7. Fisher, R.A. and L.H.C. Tippett. *Limiting forms of the frequency distribution of the largest or smallest member of a sample*. in *Mathematical Proceedings of the Cambridge Philosophical Society*. 1928. Cambridge University Press.
8. Fréchet, M. *Sur la loi de probabilité de l'écart maximum*. in *Annales de la societe Polonaise de Mathematique*. 1928. [sn].
9. Mises, R.v., *La distribution de la plus grande de n valeurs.* Rev. math. Union interbalcanique, 1936. **1**: p. 141-160.
10. Weibull, W., *The phenomenon of rupture in solids.* IVA Handlingar, 1939. **153**.
11. Fleck, N., et al., *Strain gradient plasticity: theory and experiment.* 1994. **42**(2): p. 475-487.
12. Farkas, D., et al., *Mechanical response of nanoporous gold.* 2013. **61**(9): p. 3249-3256.
13. Volkert, C., et al., *Approaching the theoretical strength in nanoporous Au.* 2006. **89**(6): p. 061920.
14. Jang, D., C. Cai, and J.R.J.N.l. Greer, *Influence of homogeneous interfaces on the strength of 500 nm diameter Cu nanopillars.* 2011. **11**(4): p. 1743-1746.
15. Biener, J., et al., *Nanoporous Au: A high yield strength material.* 2005. **97**(2): p. 024301.
16. Sun, X.-Y., et al., *Mechanical properties and scaling laws of nanoporous gold.* 2013. **113**(2): p. 023505.
17. Greer, J.R., W.C. Oliver, and W.D.J.A.M. Nix, *Size dependence of mechanical properties of gold at the micron scale in the absence of strain gradients.* 2005. **53**(6): p. 1821-1830.
18. Jennings, A., et al., *Higher compressive strengths and the Bauschinger effect in conformally passivated copper nanopillars.* 2012. **60**(8): p. 3444-3455.
19. Wu, H.J.M.R.C., *Molecular dynamics study on mechanics of metal nanowire.* 2006. **33**(1): p. 9-16.
20. Volkert, C.A. and E.T. Lilleodden, *Size effects in the deformation of sub-micron Au columns.* Philosophical Magazine, 2006. **86**(33-35): p. 5567-5579.
21. Uchic, M.D., P.A. Shade, and D.M. Dimiduk, *Plasticity of micrometer-scale single crystals in compression.* Annual Review of Materials Research, 2009. **39**: p. 361-386.
22. Kraft, O., et al., *Plasticity in confined dimensions.* Annual review of materials research, 2010. **40**: p. 293-317.

23. Greer, J.R. and J.T.M. De Hosson, *Plasticity in small-sized metallic systems: Intrinsic versus extrinsic size effect.* Progress in Materials Science, 2011. **56**(6): p. 654-724.
24. Jang, D., et al., *Deformation mechanisms in nanotwinned metal nanopillars.* Nature nanotechnology, 2012. **7**(9): p. 594.
25. Shaw, K.A., Z.L. Zhang, and N.C. MacDonald. *SCREAM I: A single mask, single-crystal silicon process for microelectromechanical structures*. in *Micro Electro Mechanical Systems, 1993, MEMS'93, Proceedings An Investigation of Micro Structures, Sensors, Actuators, Machines and Systems. IEEE.* 1993. IEEE.
26. Shi, M., et al., *Interface property of silicon nitride films grown by inductively coupled plasma chemical vapor deposition and plasma enhanced chemical vapor deposition on In0.82Al0.18As.* Infrared Physics & Technology, 2015. **71**: p. 384-388.
27. Dagata, J.A., et al., *Modification of hydrogen-passivated silicon by a scanning tunneling microscope operating in air.* Applied Physics Letters, 1990. **56**(20): p. 2001-2003.
28. Wittstock, A., et al., *Nanoporous Gold Catalysts for Selective Gas-Phase Oxidative Coupling of Methanol at Low Temperature.* Science, 2010. **327**(5963): p. 319-322.
29. Biener, J., et al., *Nanoporous Au: A high yield strength material.* Journal of Applied Physics, 2005. **97**(2): p. 024301.
30. Detsi, E., et al., *Reversible strain by physisorption in nanoporous gold.* Applied Physics Letters, 2011. **99**(8): p. 083104.
31. Hamm, C.E., et al., *Architecture and material properties of diatom shells provide effective mechanical protection.* Nature, 2003. **421**(6925): p. 841-843.
32. Chen, C.-Y., H.-X. Li, and M.E. Davis, *Studies on mesoporous materials.* Microporous Materials, 1993. **2**(1): p. 17-26.
33. Ressine, A., et al., *Macro-/Nanoporous Silicon as a Support for High-Performance Protein Microarrays.* Analytical Chemistry, 2003. **75**(24): p. 6968-6974.
34. Wada, T., et al., *Bulk-Nanoporous-Silicon Negative Electrode with Extremely High Cyclability for Lithium-Ion Batteries Prepared Using a Top-Down Process.* Nano Letters, 2014. **14**(8): p. 4505-4510.
35. Wang, G., et al., *Nanoporous Silicon Oxide Memory.* Nano Letters, 2014. **14**(8): p. 4694-4699.
36. Alvarez, S.D., et al., *The compatibility of hepatocytes with chemically modified porous silicon with reference to in vitro biosensors.* Biomaterials, 2009. **30**(1): p. 26-34.
37. Garcia, A.P., D. Sen, and M.J. Buehler, *Hierarchical Silica Nanostructures Inspired by Diatom Algae Yield Superior Deformability, Toughness, and Strength.* Metallurgical and Materials Transactions A, 2011. **42**(13): p. 3889-3897.
38. Sen, D., A.P. Garcia, and M.J. Buehler, *Mechanics of Nano-Honeycomb Silica Structures: Size-Dependent Brittle-to-Ductile Transition.* Journal of Nanomechanics and Micromechanics, 2011. **1**(4): p. 112-118.
39. Garcia, A.P. and M.J. Buehler, *Bioinspired nanoporous silicon provides great toughness at great deformability.* Computational Materials Science, 2010. **48**(2): p. 303-309.
40. Biener, J., et al., *Size Effects on the Mechanical Behavior of Nanoporous Au.* Nano Letters, 2006. **6**(10): p. 2379-2382.
41. Winter, N., et al., *Failure Mechanisms and Scaling Laws of Nanoporous Aluminum: A Computational Study* Advanced Engineering Materials, 2015: p. 632-642.
42. Plimpton, S., *Fast parallel algorithms for short-range molecular dynamics.* Journal of computational physics, 1995. **117**(1): p. 1-19.
43. Justo, J.F., et al., *Interatomic potential for silicon defects and disordered phases.* Physical Review B, 1998. **58**(5): p. 2539-2550.

44. Stillinger, F.H. and T.A. Weber, *Computer simulation of local order in condensed phases of silicon.* Physical Review B, 1985. **31**(8): p. 5262-5271.
45. Tersoff, J., *New empirical approach for the structure and energy of covalent systems.* Physical Review B, 1988. **37**(12): p. 6991-7000.
46. Hopcroft, M.A., W.D. Nix, and T.W. Kenny, *What is the Young's Modulus of Silicon?* Microelectromechanical Systems, Journal of, 2010. **19**(2): p. 229-238.
47. Moroni, L., J.R. de Wijn, and C.A. van Blitterswijk, *3D fiber-deposited scaffolds for tissue engineering: Influence of pores geometry and architecture on dynamic mechanical properties.* Biomaterials, 2006. **27**(7): p. 974-985.
48. Liu, D.-M., *Control of pore geometry on influencing the mechanical property of porous hydroxyapatite bioceramic.* Journal of Materials Science Letters, 1996. **15**(5): p. 419-421.
49. Meza, L.R., S. Das, and J.R. Greer, *Strong, lightweight, and recoverable three-dimensional ceramic nanolattices.* Science, 2014. **345**(6202): p. 1322-1326.
50. Sun, X.-Y., et al., *Mechanical properties and scaling laws of nanoporous gold.* Journal of Applied Physics, 2013. **113**(2): p. 023505.
51. Sadoc, J.F. and N. Rivier, *Foams and Emulsions*. 2013: Springer Netherlands.
52. Chokshi, A.H., et al., *On the validity of the hall-petch relationship in nanocrystalline materials.* Scripta Metallurgica, 1989. **23**(10): p. 1679-1683.
53. Nieh, T.G. and J. Wadsworth, *Hall-petch relation in nanocrystalline solids.* Scripta Metallurgica et Materialia, 1991. **25**(4): p. 955-958.
54. Becton, M. and X. Wang, *Grain-size dependence of mechanical properties in polycrystalline boron-nitride: a computational study.* Physical Chemistry Chemical Physics, 2015. **17**(34): p. 21894-21901.
55. Hodge, A.M., et al., *Scaling equation for yield strength of nanoporous open-cell foams.* Acta Materialia, 2007. **55**(4): p. 1343-1349.
56. Deshpande, V.S., N.A. Fleck, and M.F. Ashby, *Effective properties of the octet-truss lattice material.* Journal of the Mechanics and Physics of Solids, 2001. **49**(8): p. 1747-1769.
57. Schaedler, T.A., et al., *Ultralight metallic microlattices.* Science, 2011. **334**(6058): p. 962-965.
58. Fleck, N., V. Deshpande, and M. Ashby. *Micro-architectured materials: past, present and future*. in *Proceedings of the Royal Society of London A: Mathematical, Physical and Engineering Sciences*. 2010. The Royal Society.
59. Montemayor, L. and J. Greer, *Mechanical Response of Hollow Metallic Nanolattices: Combining Structural and Material Size Effects.* Journal of Applied Mechanics, 2015. **82**(7): p. 071012.
60. Greer, J.R., D. Jang, and X.W. Gu, *Exploring Deformation Mechanisms in Nanostructured Materials.* JOM, 2012. **64**(10): p. 1241-1252.
61. Chen, C.Q., Y.T. Pei, and J.T.M. De Hosson, *Effects of size on the mechanical response of metallic glasses investigated through in situ TEM bending and compression experiments.* Acta Materialia, 2010. **58**(1): p. 189-200.
62. Reischl, B., A. Kuronen, and K. Nordlund, *Nanoindentation of gold nanorods with an atomic force microscope.* Materials Research Express, 2014. **1**(4): p. 045042.
63. Tak, Y., E.R. Henderson, and K.R. Hebert, *Evolution of microscopic surface topography during passivation of aluminum.* Journal of the Electrochemical Society, 1994. **141**(6): p. 1446-1452.
64. Zhou, W., et al., *Ideal strength and structural instability of aluminum at finite temperatures.* Physical Review B, 2012. **86**(5): p. 054118.

65. Fleck, N., et al., *Strain gradient plasticity: theory and experiment.* Acta Metallurgica et Materialia, 1994. **42**(2): p. 475-487.
66. Biener, J., et al., *Nanoporous Au: A high yield strength material.* Journal of Applied Physics, 2005. **97**(2): p. 024301.
67. To, A., et al., *Ligament and joint sizes govern softening in nanoporous aluminum.* Applied Physics Letters, 2011. **98**(5): p. 051903.
68. Suárez, O.M., et al., *Fabrication of porous and nanoporous aluminum via selective dissolution of Al-Zn alloys.* Advances in Materials Science and Engineering, 2014. **2014**.
69. Qian, L. and M. Chen, *Ultrafine nanoporous gold by low-temperature dealloying and kinetics of nanopore formation.* Applied Physics Letters, 2007. **91**(8): p. 083105.
70. Provatas, N. and K. Elder, *Phase-field methods in materials science and engineering*. 2011: John Wiley & Sons.
71. Yang, W., et al., *Nanoporous Aluminum by Galvanic Replacement: Dealloying and Inward-Growth Plating.* 2018. **165**(9): p. C492-C496.
72. Daw, M.S. and M.I. Baskes, *Embedded-atom method: Derivation and application to impurities, surfaces, and other defects in metals.* Physical Review B, 1984. **29**(12): p. 6443.
73. Thiedmann, R., et al., *Stochastic 3D modeling of the GDL structure in PEMFCs based on thin section detection.* Journal of the Electrochemical Society, 2008. **155**(4): p. B391-B399.
74. Durville, D., *Numerical simulation of entangled materials mechanical properties.* Journal of materials science, 2005. **40**(22): p. 5941-5948.
75. Dirrenberger, J., S. Forest, and D. Jeulin, *Towards gigantic RVE sizes for 3D stochastic fibrous networks.* International Journal of Solids and Structures, 2014. **51**(2): p. 359-376.
76. Wirjadi, O., *Models and algorithms for image-based analysis of microstructures.* 2009.
77. Schladitz, K., et al., *Design of acoustic trim based on geometric modeling and flow simulation for non-woven.* Computational Materials Science, 2006. **38**(1): p. 56-66.
78. Peyrega, C., et al., *3D morphological modelling of a random fibrous network.* Image Analysis & Stereology, 2011. **28**(3): p. 129-141.
79. Kärkkäinen, S., et al., *A stochastic shape and orientation model for fibres with an application to carbon nanotubes.* Image Analysis & Stereology, 2012. **31**(1): p. 17-26.
80. Chapelle, L., et al. *Generation of non-overlapping fiber architecture*. in *Proceedings of the 20th International Conference on Composite Materials ICCM20 Secretariat*. 2015.
81. Altendorf, H. and D. Jeulin, *Random-walk-based stochastic modeling of three-dimensional fiber systems.* Physical Review E, 2011. **83**(4): p. 041804.
82. Altendorf, H., D. Jeulin, and F. Willot, *Influence of the fiber geometry on the macroscopic elastic and thermal properties.* International Journal of Solids and Structures, 2014. **51**(23-24): p. 3807-3822.
83. Naddeo, F., N. Cappetti, and A. Naddeo, *Automatic versatile parametric procedure for a complete FEM structural analysis of composites having cylinder-shaped reinforcing fibres.* Computational Materials Science, 2014. **81**: p. 239-245.
84. Pan, Y., *Stiffness and progressive damage analysis on random chopped fiber composite using FEM*. 2010: Rutgers The State University of New Jersey-New Brunswick.
85. Pan, Y., L. Iorga, and A.A. Pelegri, *Numerical generation of a random chopped fiber composite RVE and its elastic properties.* Composites Science and Technology, 2008. **68**(13): p. 2792-2798.

86. Fu, S.-Y. and B. Lauke, *Effects of fiber length and fiber orientation distributions on the tensile strength of short-fiber-reinforced polymers.* Composites Science and Technology, 1996. **56**(10): p. 1179-1190.
87. Luo, Y., *An efficient 3D Timoshenko beam element with consistent shape functions.* Adv. Theor. Appl. Mech, 2008. **1**(3): p. 95-106.